

**QUANTIFYING DEFORMATION IN THE EASTERN BHUTAN HIMALAYA:  
INSIGHTS FROM FLEXURAL AND THERMAL-KINEMATIC MODELS OF A  
BALANCED CROSS SECTION**

by

**Michelle Elizabeth Gilmore**

B.S. Geology, University of Pittsburgh, 2011

Submitted to the Graduate Faculty of the  
Kenneth P. Dietrich School of Arts and Sciences in partial fulfillment  
of the requirements for the degree of  
Master of Science in Geology

University of Pittsburgh

2014

UNIVERSITY OF PITTSBURGH  
KENNETH P. DIETRICH SCHOOL OF ARTS AND SCIENCES

This thesis was presented

by

Michelle Elizabeth Gilmore

It was defended on

August 8, 2014

and approved by

William Harbert, Professor, Department of Geology & Planetary Science

Brian Stewart, Associate Professor, Department of Geology & Planetary Science

Thesis Advisor: Nadine McQuarrie, Assistant Professor, Department of Geology & Planetary  
Science

Copyright © by Michelle Elizabeth Gilmore

2014

**QUANTIFYING DEFORMATION IN THE EASTERN BHUTAN HIMALAYA:  
INSIGHTS FROM FLEXURAL AND THERMAL-KINEMATIC MODELS OF A  
BALANCED CROSS SECTION**

Michelle Elizabeth Gilmore, M.S.

University of Pittsburgh, 2014

Reconstructions of a balanced geologic cross section in the Himalayan fold-thrust belt of eastern Bhutan are used in a thermal-kinematic model to understand the first order controls on thermochronometer cooling ages and track magnitude, timing and rates of deformation. We model the cross section with sequential ~10-km deformation steps and apply flexural loading and erosional offloading at each step to develop a high-resolution evolution of deformation, topography and foreland basin development in the fold-thrust belt over time. Models of topography combined with varied timing of out-of-sequence motion along the Kakhtang Thrust affect the intermediate deformational and exhumational history. We use these flexural models coupled with varying heat production values and velocities of deformation as input in the thermal-kinematic model Pecube to forward model apatite fission track (AFT), zircon (U-Th/He) (ZHe), and muscovite  $^{40}\text{Ar}/^{39}\text{Ar}$  (MAr) cooling ages during fold-thrust belt development. Comparing the predicted ages to published cooling ages along the section reveals that cooling ages are sensitive to (1) variable shortening rates, (2) how modeled topography accommodates structural uplift and flexural loading, (3) kinematic timing of fault motion, and (4) cross section geometry. Models maintaining a temporally constant deformation rate do not adequately predict cooling ages that match existing AFT, ZHe, and MAr data. Better fits to data are generated in models that use published estimates of temporally variable shortening rates. Best fits to the suite

of published cooling ages required motion along the Kakhtang Thrust both before and after duplexing of Upper Lesser Himalayan rocks, topography that can dynamically account for structural uplift and flexural loading, heat production value of  $2.5 \mu\text{W}/\text{m}^3$ , and variable deformation rates ranging from 74 mm/a to 4 mm/a. Young AFT ages (2-6 Ma) observed north of the Main Central Thrust cannot be matched in the best fitting models. We attribute this misfit to (1) a partitioning of shortening along the Kakhtang Thrust that is both kinematically and flexurally different than the models presented in this study, and/or (2) the geometry of the cross section, which may require a modified decollement north of the surface exposure of the Shumar Thrust.

## TABLE OF CONTENTS

<b>PREFACE.....</b>	<b>IX</b>
<b>1.0 INTRODUCTION.....</b>	<b>1</b>
<b>2.0 GEOLOGIC BACKGROUND .....</b>	<b>7</b>
<b>2.1 TECTONOSTRATIGRAPHY .....</b>	<b>7</b>
<b>2.1.1 Subhimalaya.....</b>	<b>8</b>
<b>2.1.2 Lesser Himalaya .....</b>	<b>8</b>
<b>2.1.3 Greater Himalaya .....</b>	<b>11</b>
<b>2.1.4 Tethyan Himalaya .....</b>	<b>12</b>
<b>2.2 THERMOCHRONOLOGIC DATA .....</b>	<b>12</b>
<b>3.0 METHODS .....</b>	<b>14</b>
<b>3.1 KINEMATIC MODEL .....</b>	<b>14</b>
<b>3.2 MODELING WITH FLEXURAL ISOSTACY AND TOPOGRAPHY.....</b>	<b>15</b>
<b>3.3 THERMAL MODEL: PECUBE .....</b>	<b>21</b>
<b>4.0 RESULTS .....</b>	<b>24</b>
<b>4.1 FLEXURAL ISOSTACY MODEL.....</b>	<b>24</b>
<b>4.1.1 Isostatic responses to differing KT timing .....</b>	<b>24</b>
<b>4.1.2 Topographic sensitivity in flexural models .....</b>	<b>26</b>
<b>4.2 PECUBE PREDICTIVE COOLING AGE MODEL.....</b>	<b>30</b>

4.2.1	Heat production sensitivity .....	30
4.2.2	Velocity variation.....	32
4.2.3	Topographic sensitivity .....	36
4.2.4	Kinematic variation.....	38
5.0	DISCUSSION .....	41
5.1	EVALUATING AGREEMENT BETWEEN MODELED AND PUBLISHED DATA.....	41
5.1.1	Possible geometric solutions .....	42
5.1.2	Possible flexural and topographic solutions.....	43
5.2	DEFORMATION TIMING AND VELOCITY RANGES FITTING PUBLISHED DATA.....	45
5.3	COMPARISON TO OTHER THERMAL-KINEMATIC MODELING ALONG THE TRASHIGANG SECTION.....	47
6.0	CONCLUSIONS .....	49
	APPENDIX A .....	51
	BIBLIOGRAPHY .....	56

## LIST OF TABLES

Table 1 Comparison of the published cross section to flexural model output.....	25
Table A-1 Previously published thermochronologic data .....	52
Table A-2 Tested combinations of flexural and thermal-kinematic models inputs.....	53

## LIST OF FIGURES

Figure 1 Thermal-kinematic modeling approaches .....	3
Figure 2 Simplified geologic map of Bhutan and surrounding region .....	4
Figure 3 Geologic map of part of eastern Bhutan with published thermochronometer data.....	10
Figure 4 Deformed and restored Trashigang cross section.....	10
Figure 5 Published cooling data and observed topography plotted by distance along section.....	13
Figure 6 Net slip applied along each fault in the Trashigang cross section.....	14
Figure 7 Sequentially deformed Trashigang cross section with kinematic variations shown .....	17
Figure 8 Flexural modeling steps with Template and Python Topography.....	18
Figure 9 Sample horizontal and vertical velocity fields .....	20
Figure 10 Modeled topographies of the final deformed cross sections .....	27
Figure 11 Published Trashigang section compared to flexural model output: Split KT .....	28
Figure 12 Pecube output: variable heat production .....	32
Figure 13 Pecube output: variable velocities .....	34
Figure 14 Pecube output: variable topography models.....	36
Figure 15 Pecube output: variable kinematic scenarios.....	38
Figure 16 Pecube output: Split KT, Template Topography, Velocity B, $A_0 = 2.5 \mu\text{W}/\text{m}^3$ .....	42
Figure 17 Pecube output: Early KT, Template Topography, Velocity B, $A_0 = 2.5 \mu\text{W}/\text{m}^3$ .....	44

## PREFACE

Funding for this research was provided by the University of Pittsburgh and the National Science Foundation (NSF #0948449).

This work would not have been possible without the help of many people in Pittsburgh and beyond. I would like to acknowledge Todd Ehlers and Willi Kappler (U. of Tübingen) for their guidance throughout the Pecube modeling process. I am grateful for those who helped with data compilation: Adam Rak and Robert McDermott at the University of Pittsburgh, as well as Sean Long (UN-Reno). And I appreciate the help that Alison Graettinger (U. at Buffalo) and Taya Flaherty offered in Pitt's Microanalysis Lab, along with Janelle Thumma who assisted with both microanalysis and flexural model workflow. I would also like to thank members and visitors of Dr. McQuarrie's research group for their support, particularly Nathan Eichelberger (Princeton) and Nicholas Perez (UT-Austin) for feedback on cross sections and presentations.

I thank my committee members for their wealth of guidance and all of their comments. Bill Harbert and Brian Stewart helped strengthen the quality of my work and build my confidence and knowledge. I am especially grateful for my advisor, Nadine McQuarrie, for guidance over the past two years and for providing immeasurable support in all aspects of this and other projects. Thank you for sharing your knowledge and experience with me, and for encouraging me to expand my graduate experience through conferences and workshops. You

have helped me grow as a capable and confident scientist, and as a well-rounded researcher, writer, and presenter.

Finally, I thank my family and friends for supporting me during my time in graduate school. I could not have completed this undertaking without the love from my parents, brothers, aunts, uncles, and grandparents. I give great thanks to Michael Blonski for his endless encouragement and delicious dinners, especially over the last several months of research and writing, and to Stacey Kuznetsov for sharing optimism and countless espressos with me.

## 1.0 INTRODUCTION

Thermochronometers can preserve information regarding age of burial, deformation, and exhumation in compressional systems. These ages are set as a function of the timing, magnitude, and rate of exhumation in fold thrust belts [e.g., Ehlers and Farley, 2003]. Thermal models that predict thermochronometer cooling ages indicate that fault geometry, particularly the location of ramps, localize exhumation processes [Whipp et al., 2007; Robert et al., 2009; Coutand et al., 2014]. Several studies have shown cooling ages to be the most sensitive to vertical exhumation processes, such as structural uplift over a fault ramp. [Whipp et al., 2007; Robert et al., 2009; Coutand et al., 2014]. Because of this, several hundred kilometers of horizontal shortening, a phenomenon commonly observed in fold-thrust belts, may occur without a significant thermal cooling signal [e.g., Batt and Brandon, 2002; Huntington et al., 2007; Whipp et al., 2007]. The shape of subsurface isotherms and the cooling history of minerals are also controlled by locations of focused erosion through time and the resulting evolution of topography. [Ehlers and Farley, 2003]. However, how topography has changed with time remains a largely unknown component in the evolution of any fold-thrust belt.

Evaluating a suite of thermochronologic ages in the Himalaya, using either simple 1-dimensional or more complicated 2-D thermal models, several authors have identified temporally and spatially variable rates of denudation across the orogen [e.g., Thiede and Ehlers, 2013; Thiede et al., 2009; Adlakha et al., 2013; Robert et al., 2009; Coutand et al.; 2014]. Sequential

cross section deformation in combination with thermochronologic data has also been used to estimate variable magnitudes and rates of deformation, erosion, and deposition in Himalayan fold-thrust belt development [Robinson and McQuarrie, 2012; Long et al. 2012, McQuarrie et al. 2014]. However these 1-D and 2-D models commonly simplify the relationship between deformation, exhumation, and rock cooling. Thermal advection associated with motion along faults of nonuniform dips (i.e., where ramps exist), as well as localized areas of heightened erosion, perturb isotherms enough that cooling and exhumation curves may be decoupled in the upper 10 km of the crust [Batt and Brandon, 2002; Huntington et al., 2007; Coutand, 2014].

Other 2- and 3-dimensional thermal-kinematic models attempting to account for the effects of deformation and erosion on thermochronometer cooling have been used to calculate rates of erosion, cooling, and fault activity in the Himalaya [Celerier et al., 2009; Herman et al., 2010; Coutand et al., 2014]. These models rely on a pinned fault, with foreland-ward motion from the over-riding plate and hinterland-ward motion from underthrusting of the Indian Plate (Figure 1). New material is incorporated into the hanging wall of the Main Himalayan Thrust (MHT), by the transfer of material from below the fault to above the fault. This is mostly concentrated at a ramp in the MHT, but some accretion from the underlying plate to the overlying plate is included along the entire fault length [Herman et al., 2010]. The rate of overthrusting of the hanging wall and the rate of underthrusting of the footwall sum to the net convergence velocity. Although the partitioning of velocity into the over-riding plate and the under-riding plate can vary, the net velocity, or convergence, does not, and fault geometry is kept static over time [Celerier et al., 2009; Herman et al., 2010; Coutand et al., 2014].

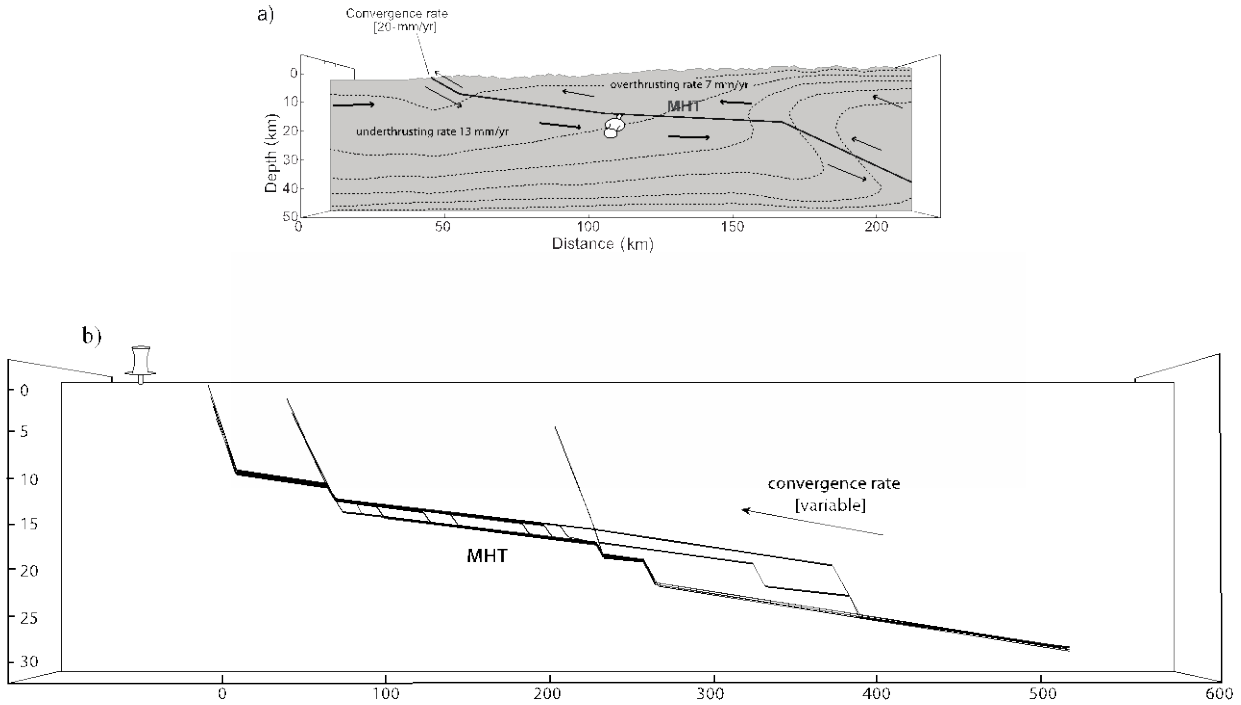


**Figure 1** Thermal-kinematic modeling approaches of (a) previous studies in the Himalaya and (b) the approach used in this study, from McQuarrie and Ehlers [in prep]. In subfigure (a) the model partitions convergence into an overthrusting rate and an underthrusting rate on either side of a static (pinned) fault, the Main Himalayan Thrust (MHT). Dotted lines represent the modeled thermal field. Subfigure (b) has solid lines that illustrate the changing position of the MHT and how the location and geometry of footwall ramps change across the model. The footwall of the fault is pinned in the model, and the hanging wall of the fault moves at a net convergence rate that can vary with time.

In this study, we create sequential reconstructions of a balanced cross section from the Trashigang region of Bhutan [Long et al., 2011a] (Figure 2) to evaluate the geometry and crustal shortening of the Himalayan fold-thrust. By accounting for deformation and associated isostatic loading, plus unloading from erosion, we can use sequential cross sections to produce a record of syn-deformational exhumation and deposition. This flexural model also produces a displacement field that predicts the pathways of rocks toward the surface. The displacement field is input into

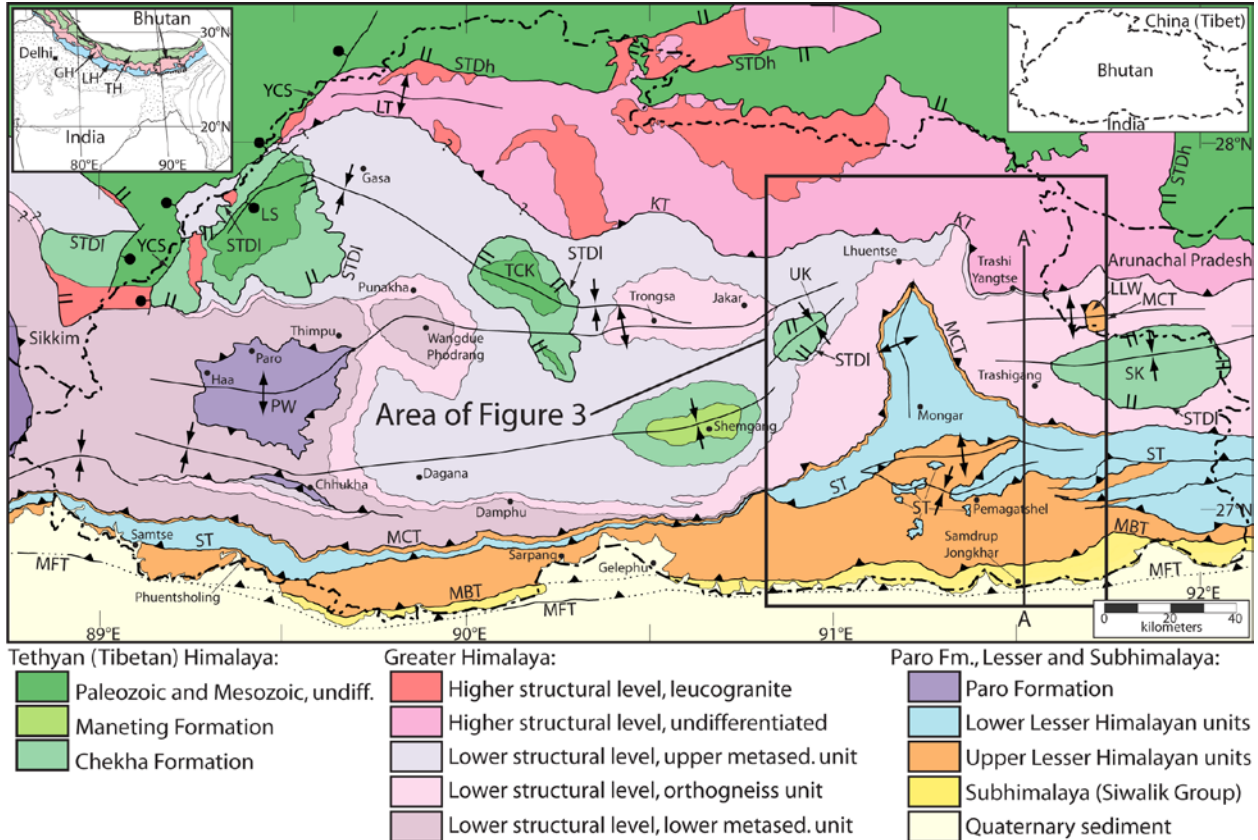


**Figure 2** Simplified geologic map of Bhutan and surrounding region illustrating tectonostratigraphy, from Long et al., [2011b]. Area of Figure 3 is shown, along with line A-A' for the Trashigang cross section (Figure 4). Top right inset shows the geographic borders of Bhutan and surrounding countries. Top left inset shows a generalized geologic map of the central and eastern Himalayan orogen (modified from Gansser [1983]). Abbreviations in inset are GH: Greater Himalaya, LH: Lesser Himalaya, TH: Tethyan Himalaya: Abbreviations of structures from north to south: YCS: Yadong Cross-Structure, STDh: structurally higher South Tibetan Detachment, LT: Laya thrust, KT: Kakhtang Thrust, STDI: structurally lower South Tibetan Detachment, MCT: Main Central Thrust, ST: Shumar Thrust MBT: Main Boundary Thrust, MFT: Main Frontal Thrust; (3) windows and klippen from west to east: LS: Lingshi syncline, PW: Paro window, TCK: Tang Chu klippe, UK: Ura klippe, SK: Sakteng klippe, LLW: Lum La window. WGS84 datum.

a 2-D thermal-kinematic model (Pecube) [Braun, 2003; Whipp et al., 2009] that calculates cooling ages across the cross section for each deformation step, creating a high-resolution spatiotemporal cooling history of the fold-thrust belt. We compare the predicted ages from Pecube to the measured thermochronometer data available in eastern Bhutan along the Trashigang cross section [Coutand et al., 2014; Long et al., 2012; Grujic et al., 2006; Stüwe and Foster, 2001]. We address the problems associated with previous models by using a flexural model that pins the footwall of the fold-thrust belt in place and allows us to model a dynamic detachment that can migrate across the fold-thrust belt over time (Figure 1). By allowing the decollement to change with time, we can incorporate data typically ignored in thermal modeling such as changes in footwall geometry predicted by balanced cross sections. Pinning the footwall also permits us to assign absolute magnitudes and rates of deformation to material in the hanging wall of the Main Himalayan Thrust. Through varying the locations, ages, and rate of faulting, the linked kinematic and thermal models allow us to determine permissible magnitudes, timing, and rates of deformation in the eastern Bhutanese Himalaya.

We use three different kinematic scenarios of out-of-sequence faulting along the Kakhtang Thrust (KT) in the flexural models. These kinematic and flexural models are input in the thermal-kinematic model to evaluate the differences in predicted ages due to different possible times of out-of-sequence faulting. With varying degrees of topographic detail and fit to observed topography, we also test the topographic sensitivity of the thermal-kinematic model in generating accurate predictive output of thermochronometer data, as well as a general best fit to known parameters of observed topography, surface geology, foreland basin thickness, and decollement angle. Finally we evaluate several velocities and ages of fault motion to determine if deformation rates have in fact been constant during fold-thrust belt evolution, and how

shortening rates may vary as the Himalayan fold thrust belt in Eastern Bhutan develops, in order to best fit published cooling ages. By studying all of these parameters' influences on cooling ages in our coupled flexural and thermal-kinematic modeling approach, we can better understand the pathway from undeformed in the subsurface to deformed on the surface, and quantify this linked kinematic, erosional, and thermal history for the Himalayan fold-thrust belt in Eastern Bhutan.

## **2.0 GEOLOGIC BACKGROUND**

The Himalayan orogen is regarded as the modern model for continent-continent collision zones and shares features found at any convergent boundary. Collision of the Indian Plate with the Asian Plate began c. 50-55 Ma [e.g., Patriat and Achache, 1984; Yin and Harrison, 2000; Hodges, 2000]. Estimates for the initiation of motion on the Main Central Thrust (MCT), range from ~25 to 20 Ma [e.g., DeCelles et al., 2001; Long et al., 2012; McQuarrie et al., 2014]. The Himalayan fold-thrust belt is composed of south-verging structures and extends from the suture between India and Asia in southern Tibet southward into northern India, Bhutan, and Nepal. It comprises igneous, sedimentary, and metasedimentary rocks of Paleoproterozoic to Quaternary age [Gansser, 1964; Powell and Conaghan, 1973; LeFort, 1975; Mattauer, 1986; Hodges, 2000; DeCelles et al., 2002; Yin, 2006].

### **2.1 TECTONOSTRATIGRAPHY**

The Himalaya fold-thrust belt is divided into four tectonostratigraphic zones, typically separated by major fault structures that span across the entire thrust belt. From south to north, these are the Subhimalaya (SH), Lesser Himalaya (LH), Greater Himalaya (GH), and Tethyan Himalaya (TH) (Figure 2). All of these units were derived from rocks originally deposited on the Indian Plate [Heim and Gansser, 1939; Gansser, 1964]. This section will focus on generalized aspects of each

tectonostratigraphic zone and details of each zone with regard to their occurrence in eastern Bhutan and along the Trashigang cross section that is used in this study [Long et al., 2011a].

### **2.1.1 Subhimalaya**

The Subhimalayan zone is located north of the Main Frontal Thrust (MFT) and composed of synorogenic sedimentary deposits from the Himalayan foreland basin prior to MFT motion. The MFT is interpreted as the most recent expression of the Main Himalayan Thrust (MHT). In Bhutan the MFT emplaces a single thrust sheet of SH units over modern foreland basin deposits [Gansser, 1983; Long et al., 2011a] (Figure 3). SH rocks consist of the Siwalik Group, composed of Miocene-Pliocene siltstone, sandstone, and conglomerate. The northern end of the SH zone rests in the footwall of the Main Boundary Thrust (MBT) (Figure 4).

### **2.1.2 Lesser Himalaya**

The Lesser Himalayan zone consists of a package of younger rock units, collectively grouped as the Upper LH, and a suite of older formations comprising the Lower LH [Long et al., 2011a] (Figures 2 and 3).

The youngest unit of the Upper LH, the Gondwana succession, is exposed north of the SH zone in the hanging wall of the MBT (Figure 3). The Gondwana comprises Permian sandstone, carbonaceous shale and siltstone, and coal [McQuarrie et al, 2008; Long et al., 2011b]. Stratigraphically below this is Permian diamictite of the Diuri Formation (Figure 3). The Gondwana and Diuri have been carried in multiple thrust sheets in southeastern Bhutan [Long et al., 2011a]. North of these Permian units is a duplex of the Neoproterozoic-Cambrian Baxa

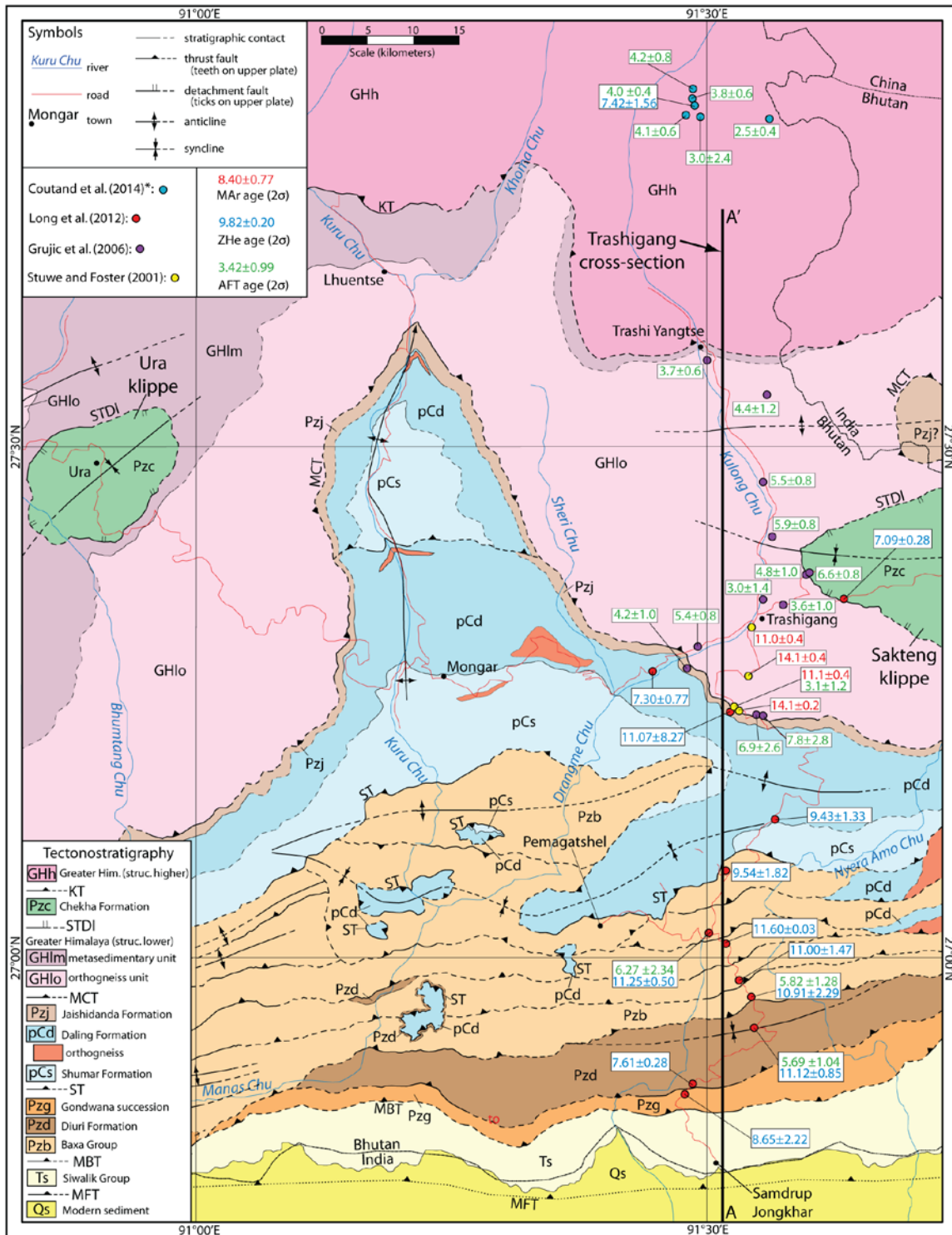


**Figure 3 (previous page)** Geologic map of part of eastern Bhutan, after Long et al. [2012]. See Figure 2 caption for structure abbreviations. The Trashigang cross section's (Figure 4) line of section is shown (A-A'). Blue circles mark AFT and ZHe data from Coutand et al. [2014] that has been projected 27 km SE at 129 degrees. Red circles mark locations of AFT and ZHe samples from Long et al. [2012]. Purple circles mark AFT ages from Grujic et al. [2006]. Yellow circles mark MAr and AFT ages from Stüwe and Foster [2001]. Red ages are MAr, blue ages are ZHe, and green ages are AFT. WGS84 datum.

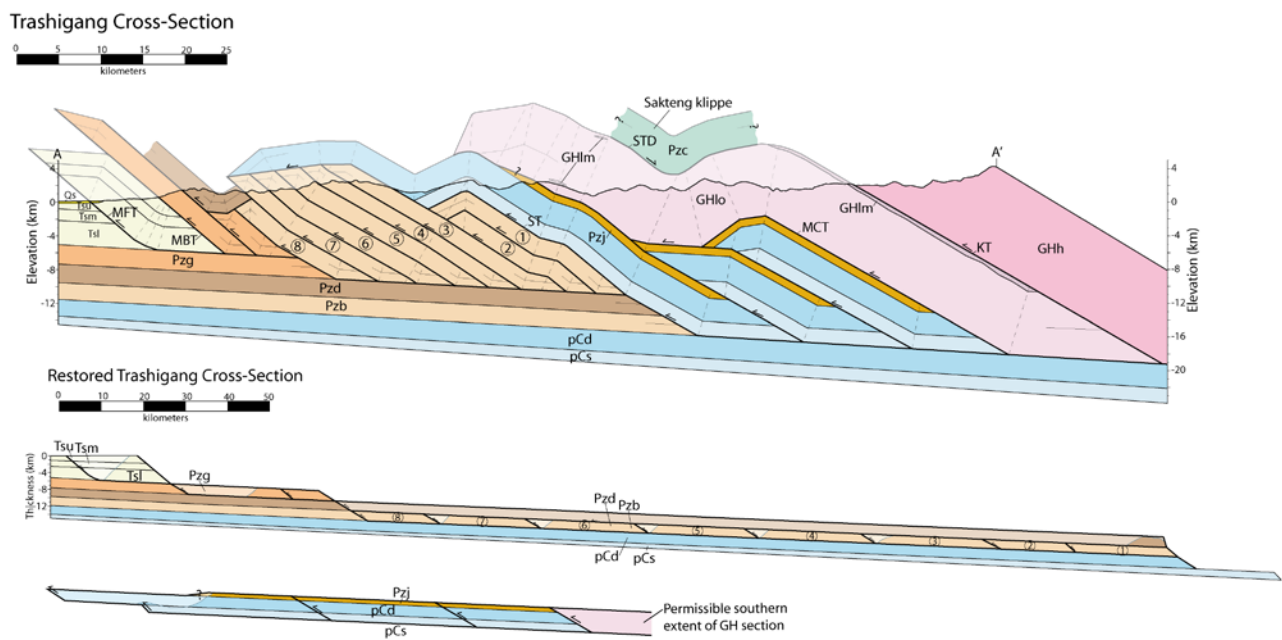


**Figure 4** Deformed and restored Trashigang cross section, simplified from Long et al. [2011a]. Unit abbreviations are shown in the stratigraphic column of Figure 3. Lightened area in the deformed cross section illustrates material eroded above the modern topographic surface. Abbreviations of structures from north (right) to south (left): STD: South Tibetan detachment, KT: Kakhtang thrust, MCT: Main Central thrust, ST: Shumar thrust, MBT: Main Boundary thrust, MFT: Main Frontal thrust. Lower LH duplex containing pCs, pCd, and Pzj is shown below the GH synform. Numbers on Pzb represent kinematic order of faults in the Upper LH (Baxa) duplex with the Shumar Thrust (ST) as the roof thrust.

Group (Figure 3), composed of interbedded metasedimentary quartzite, dolomite, and phyllite [McQuarrie et al., 2008; Long et al., 2011b]. Multiple horses of the Baxa Group are repeated in this Upper LH duplex with the Shumar Thrust (ST), exposed immediately to the north, interpreted as the roof thrust of the system (Figures 3 and 4).

In the hanging wall of the Shumar Thrust, the Paleoproterozoic Daling-Shumar Group is exposed, overlain by the stratigraphically unconformable Neoproterozoic-Ordovician Jashidanda Formation (Figure 3). The Jashidanda Formation consists of quartzite and schist, while the Daling and Shumar units are respectively composed of phyllite-schist and quartzite [McQuarrie et al., 2008; Long et al., 2011b]. These units are repeated multiple times to form the Lower LH duplex, based on outcrop relationships exposed east of the Trashigang cross section, with the Main Central Thrust (MCT) acting as the roof thrust (Figure 4).

### **2.1.3 Greater Himalaya**

The MCT divides the southern Lesser Himalayan zone from the Greater Himalayan zone located north of the MCT [Heim and Gansser, 1939; Gansser, 1964]. The GH zone is divided into two structural levels: the lower GH is above the MCT but below the Kakhtang Thrust (KT), while the higher GH unit sits above the KT [Grujic et al., 2002] (Figure 3). The lower GH section contains Cambrian-Ordovician granitic orthogneiss capped by metasedimentary units [Long and McQuarrie, 2010; Long et al., 2011a], while the structurally higher section of GH consists of Cambrian-Ordovician migmatitic orthogneiss and metasedimentary units with Miocene leucogranite intrusions [e.g. Gansser, 1983; Davidson et al., 1997; Grujic et al., 2002]. Based on available mapping data [Long et al., 2011b], hanging walls for both GH sections are interpreted

to have eroded hanging wall cutoffs, and regional-scale antiforms and synforms are interpreted to be a result of underlying lower LH duplex formation [Long et al., 2011a] (Figure 4).

#### **2.1.4 Tethyan Himalaya**

The TH zone is mapped as both stratigraphically and structurally above the GH in Bhutan [e.g., Grujic et al., 2002; Gansser, 1983; Bhargava et al., 1995; Long et al., 2011a]. The structural contact for TH units adjacent to GH rocks is a normal-sense, top-to-the-north shear zone termed the South Tibetan Detachment (STD) [Grujic et al., 2002] (Figures 2 and 3). A more limited number of conformable stratigraphic contacts are isolated in central Bhutan [Long and McQuarrie, 2010]. TH rocks of the Chekha Formation are greenschist facies metasedimentary quartzite and schist. Eroded Chekha Formation is shown above modern topography in the Trashigang cross section (Figure 4) based on its proximity to the Sakteng Klippe preserved to the east (Figures 2 and 3).

## **2.2 THERMOCHRONOLOGIC DATA**

The variety of lithologies in the Himalaya fold-thrust belt, paired with high erosion rates, promote the utility of a suite of thermochronologic data. Available chronometers in eastern Bhutan include muscovite  $^{40}\text{Ar}/^{39}\text{Ar}$  (MAr), zircon (U-Th)/He (ZHe), and apatite fission track (AFT), which can be used together to estimate changes in rates of erosion and deformation over the space and time of the thrust belt [e.g., Thiede et al., 2009; Long et al., 2012; Thiede and Ehlers, 2013; Adlakha et al., 2013; McQuarrie et al., 2014]. Data used in this study are spatially

presented in Figure 3, and plotted by age and distance along the Trashigang cross section in Figure 5. AFT and ZHe data published by Coutand et al. [2014] have been projected 27 km along a line trending 129 degrees SE, maintaining the dataset's original distance from the KT and STD, to better complete available data in the northern end of the section (Figure 3). Other thermochronologic data used in this study were previously compiled by Long et al. [2012]. Location, elevation, and thermochronometer data for each sample is listed in Table A-1.

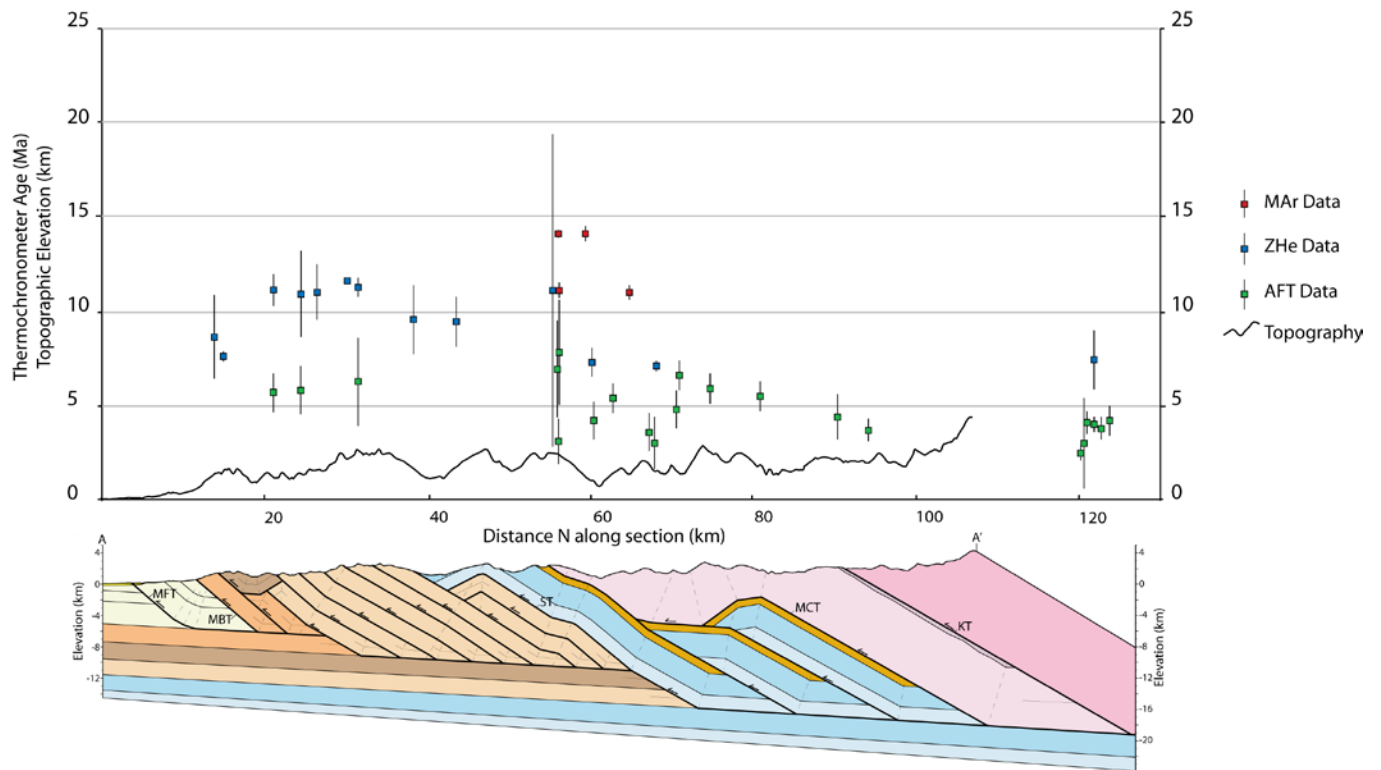


**Figure 5** Published MAR (red), ZHe (blue), and AFT (green) cooling age data and observed topography (black) plotted by distance along cross section. Deformed Trashigang cross section simplified from Long et al. [2011b] is shown and horizontally scaled to the age data. Reported ZHe ages are an average of the reported ZHe dates for each rock sample. Bars shown for ZHe are  $2\sigma$  variability ranges based on the variation in dates reported for sample. Error bars for MAR and AFT are  $2\sigma$  analytical errors.

### 3.0 METHODS

#### 3.1 KINEMATIC MODEL

Long et al. [2011a] published a balanced geometric solution for the structural subsurface in the Trashigang region of Bhutan (Figure 4). To develop a kinematic model, we used the structural modeling software Move® by Midland Valley Exploration™ to sequentially deform the restored Trashigang cross section using slip amounts based on the deformed cross section. This workflow tests the kinematic viability of the cross section. Final slip amounts for motion applied along each fault are shown in Figure 6.

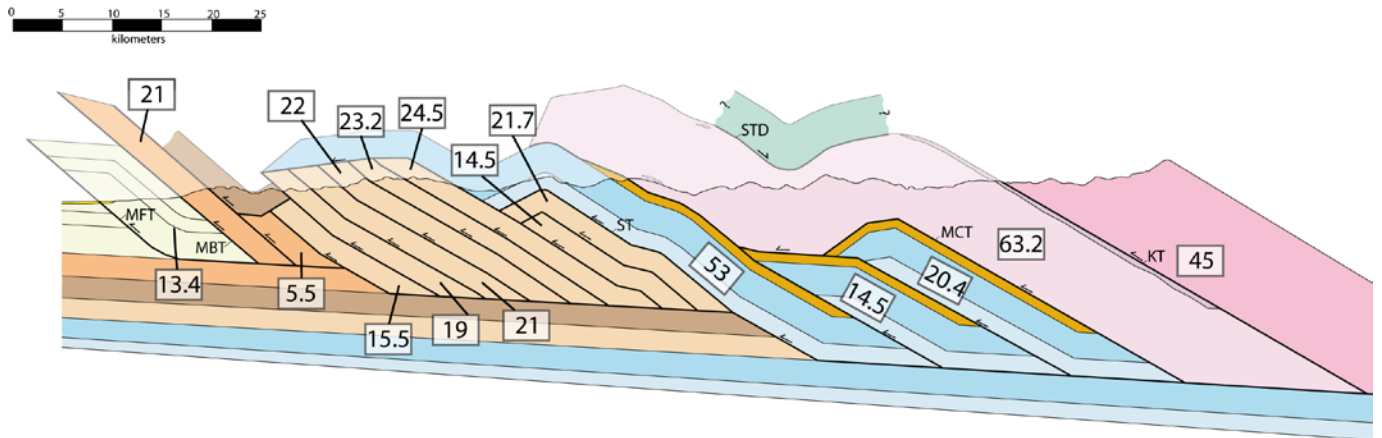


**Figure 6** Simplified Trashigang cross section shown with net slip direction and magnitude of shortening (km) applied to each fault in the kinematic and flexural models.

It is known that out-of-sequence thrusting along the Kakhtang Thrust occurred more recently than motion on the MCT [Davidson et al., 1997; Grujic et al., 2002; Hollister and Grujic, 2006]. However, debate remains regarding the magnitude and timing of slip along the KT. The range of estimates for periods of out-of-sequence thrusting in the Himalaya are 22.5-18.5 Ma [Hodges et al., 1996], 14-10 Ma [Grujic et al., 2002], 4.9-1.5 Ma [Jain et al., 2000] and from Late Pliocene to even Holocene Period [Burbank, 2005, Wobus et al., 2003]. We tested three kinematic scenarios differing in relative timing of KT motion (Figure 7). Early KT places the entire 45 km of motion along the KT after motion on the Shumar Thrust (Figure 7c.1). Split KT models two separate stages of out-of-sequence thrusting, with 25 km of motion before the Baxa duplex begins forming and 20 km of motion after Upper LH duplex deformation is complete (Figure 7c.2). Late KT places all motion along the KT near the end of Baxa duplex formation, before the last horse of the duplex is deformed, similar to the proposed model of sequential deformation by Long et al. [2012] (Figure 7c.3).

### **3.2 MODELING WITH FLEXURAL ISOSTASY AND TOPOGRAPHY**

Once the deformed Trashigang cross section was accurately reproduced, we again sequentially deformed the cross section and this time included isostatic response to deformational loading and erosional offloading, producing a record of syn-deformational exhumation and deposition (Figure 8). To model isostatic response, we used three different topographic scenarios with varying degrees of resolution. These topographies tested the sensitivity of the flexural model in creating a best fitting match to modern exposed surface geology, foreland basin thickness, and decollement dip. The three topographic models were also evaluated in thermal-kinematic model

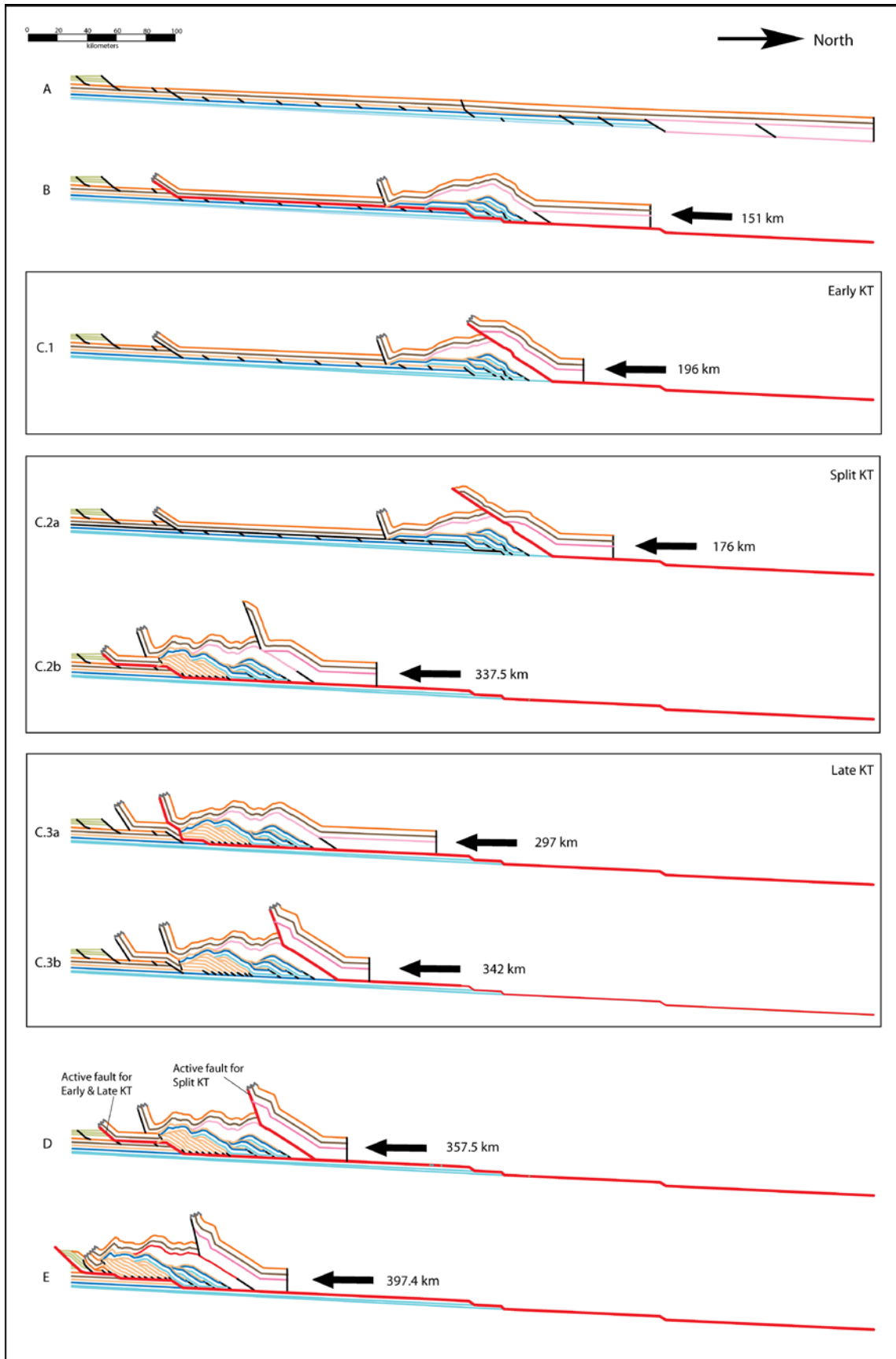


**Figure 7 (previous page)** Sequentially deformed Trashigang cross section with three kinematic scenarios of motion along the Kakhtang Thrust. Net slip amounts are shown for each subfigure. (A) shows the restored section used in the model. (B) shows the cross section after deformation along the MCT and ST. Three models of (C) are shown representing different relative timings of out-of-sequence KT motion - Early KT (C.1), Split KT (C.2), and Late KT (C.3) - and Upper LH duplexing. (D) illustrates how all cross sections appear once KT motion and Upper LH duplexing are complete. Note that Split KT has a different active fault compared to Early and Late KT scenarios in (D). (E) is the final deformed cross section following MBT and MFT activity.

Pecube to determine the sensitivity of the predicted thermochronometric data to each topographic scenario.

The “No Topography” scenario (not shown in Fig. 8) used a constant topographic line at 0 km elevation across the entire length and time of the section. We also tested a “Template Topography” similar to the modern topographic gradient of Bhutan (Duncan et al., 2003) that maintains a steep gradient in the first 20 km behind the active deformation front followed by a more gently sloping 2 degree topography (Figure 8a). With Template Topography, the location of the deformation front is adjusted throughout the sequential development of the fold-thrust belt, but the topographic geometry remains the same north of the deformation front. This topography therefore does not generally account for localized structural uplift and changes to active fault geometry when the deformation front is kept constant (Figure 8a.4). The third topography calculates a new topographic profile for each loaded ~10-km deformational step using a Python-based computer script (Python Topography) (Figure 8b). This topography maintains a constant taper angle defined by the user (i.e. 2 degrees). New topography is generated using the 2° slope as a guide where active uplift is occurring, and in regions of no active uplift the topography follows existing topography and generates lower elevations where dip-slopes, flats, and basins exist (Figure 8b.4).

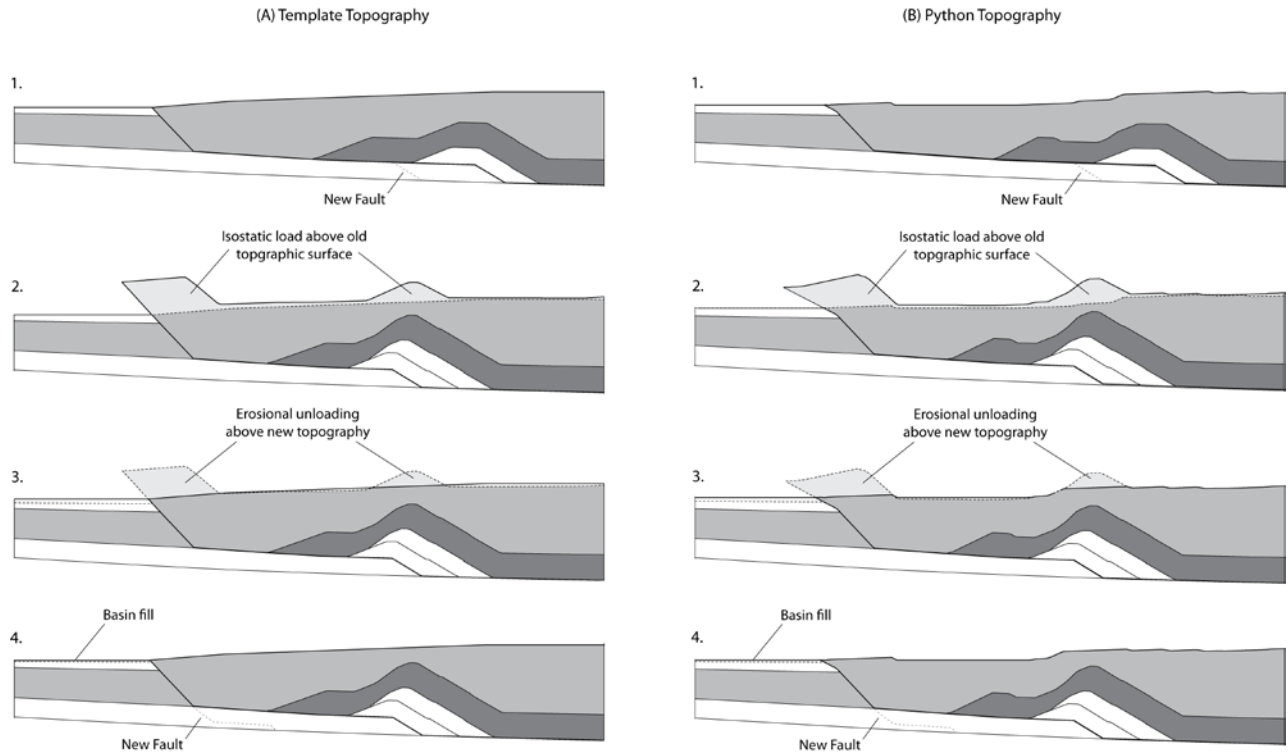


**Figure 8** Flexural modeling steps with (a) Template Topography and (b) Python Topography. Steps illustrate final topography and subsurface prior to next fault step (1) followed by the deformed section resulting from fault slip (2). In (2) the lightest gray area is the material between the old topographic surface and the deformed topography that loads the cross section. Following this, new topography is input (3) and the light gray area is now the material between the deformed, loaded topography and new topography that erosionally offloads the section. Then the new topography is reinserted, and net subsidence and deposition in the foreland basin is observed (4).

The modeled topography is the most different during periods of out-of-sequence thrusting because of how each model accounts for structural uplift and isostatic loading of material south of the Kakhtang Thrust. Because Python Topography model calculates new topography based on the loaded profile of deformed topography (Figure 8), out-of-sequence thrusting still actively erodes material between the out-of-sequence thrust and the deformation front while burying material that subsides below sea level. The static nature of Template Topography in front of the KT does not lower topography during KT motion and results in periods of non-erosion and burial

at this time. This difference is minimal enough to result in similar final flexural model output with the same input parameters (Section 4.1) but causes different erosional histories of intermediate steps between the restored and final deformed section.

Variables of effective elastic thickness (EET), crustal density, and initial decollement dip were adjusted to achieve a best fit for all 7 flexural models with priority placed on matching surface geology. Young's modulus and mantle density were held constant at 70 GPa and 3.3 g/cm<sup>3</sup>. Geophysical estimates of EET in Bhutan are at maximum 25 km [Hammer et al., 2013], increasing westward along strike to values of 40-75 km in Nepal [Berthet et al., 2013]. Low EET values in our flexural model resulted in undesired forebulge erosion in the foreland basin because of shorter flexural wavelength, as well as steeper decollement dips that were poorer fits to the 4° dip of the published Trashigang cross section [Long et al., 2011a]. Our best fits to observed surface geology, foreland basin depth, and decollement dip used an EET of 65 km for all kinematic and topographic combinations. Density values for rocks in the Himalaya of eastern India range are 2.45 g/cm<sup>3</sup> in the Siwaliks zone, 2.7-2.89 g/cm<sup>3</sup> in the Lesser Himalaya, 2.75-2.91 g/cm<sup>3</sup> in the Greater Himalaya, and 2.65-2.7 g/cm<sup>3</sup> in the Tethyan Himalaya [Mitra et al., 2005]. Our crustal density value for models with Template and Python topographies is slightly lower than most of these observed ranges (2.6 g/cm<sup>3</sup>). Our No Topography scenario required a much higher crustal density (3.2 g/cm<sup>3</sup>) to provide sufficient load when no material is preserved above sea level.

Following a best-fit creation for each flexural model, we added a 0.5 km-resolution grid of points that spans the entire length and depth of the section. These points represent particles in the subsurface that will be numerically deformed and exhumed. The cross section is deformed in increments averaging ~10 km, isolating motion along each fault. This allows for the generation

of high-resolution displacement vectors highlighting how the kinematics of the system evolve in ~10 km increments. The displacement field is turned into a velocity field by assigning an age to each step (Figure 9).

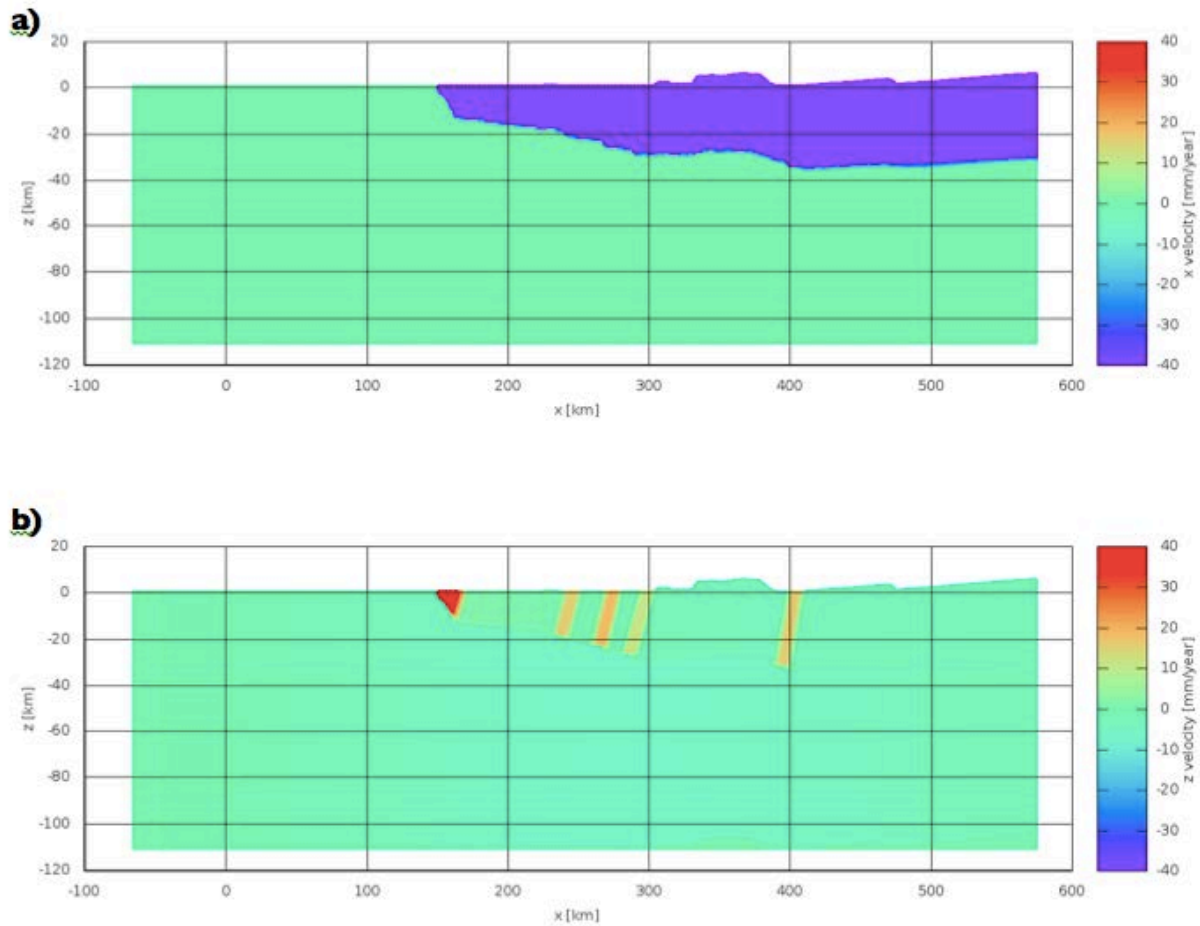


**Figure 9** Sample horizontal (a) and vertical (b) velocity fields from an intermediate step in the flexural model. Velocity of material in the footwall of the model remains at 0 mm/a, while horizontal and vertical velocities vary based on assigned ages and rates of deformation. Vertical velocity (b) increases when material moves over ramps in the decollement.

### 3.3 THERMAL MODEL: PECUBE

The velocity field and topography for each increment of deformation, after isostasy and erosion has been applied, is input into the thermal-kinematic predictive model Pecube [Braun, 2003; Whipp et al., 2009]. The thermal-kinematic model functions as: (1) a kinematic model that uses fault geometries and high-resolution point tracing to calculate rock transport (advection) velocities; (2) a thermal model that calculates a thermal field using fault motion, erosion above the topographic surface, thermal rock properties, and thermal boundary conditions; and (3) a set of age prediction algorithms that calculate a suite of thermochronometer ages for material at the topographic surface for each deformation step using the thermal histories of particles as they are exhumed and cooled from depth to the model surface [Coutand et al., 2014]. The model predicts the cooling ages of rock samples that could be collected at each deformation step, up to the modern deformed cross section geometry.

Calculated values of radiogenic heat production in the Himalaya span a broad range of values. A low heat production estimate of  $0.8 \mu\text{W}/\text{m}^3$  for the entire Indian Shield was calculated based on observed low heat flow [Ray and Rao, 2000], but localized values were estimated as high as  $1.5\text{-}5.5 \mu\text{W}/\text{m}^3$  due to the abundance of potassium, uranium, and thorium in granitic and gneissic rocks [Menon et al., 2003]. Similar ranges of heat production values ( $1.5$  to  $6.0 \mu\text{W}/\text{m}^3$ , with clustering around  $4 \mu\text{W}/\text{m}^3$ ) have also been found for Greater Himalayan rocks [e.g., England et al., 1992; Whipp et al., 2007]. Samples measured from the Garhwal Himalaya, west of Nepal, found gneissic and metabasic rocks of the GH to have thermal conductivity values between  $1.5$  and  $3.5 \text{ W}/\text{mK}$ , averaging  $2.5 \text{ W}/\text{mK}$ , and quartzite values higher at  $4\text{-}8 \text{ W}/\text{mK}$  [Ray et al., 2007]. Herman et al. [2010] concluded a best fitting heat production value of  $2.2 \mu\text{W}/\text{m}^3$  in their own thermal-kinematic model. In this study we tested radiogenic heat production values

ranging from 3.5 to 1.0  $\mu\text{W}/\text{m}^3$  while holding velocity constant, and from 3.5-2.25  $\mu\text{W}/\text{m}^3$  for variable velocity tests (Table A-2).

A variety of deformation ages and velocities were tested to predict AFT, ZHe, and MAR cooling dates. A constant deformation velocity of 17.28 mm/a was calculated using 23 Ma as the timing of MCT initiation [Long et al., 2012], and applied to the model to test if a generalized long-term rate of shortening, often employed in other thermal-kinematic models for the Himalaya, can adequately reproduce published MAR, ZHe and AFT cooling ages. This rate is comparable to estimates of modern convergence for the Himalaya from ~15-25 mm/a [Bilham et al., 1997; Larson et al., 1999; Banerjee and Burgmann, 2002; Zhang et al., 2004; Bettinelli et al., 2006; Banerjee et al., 2008] and other studies calculating long-term rates of shortening [DeCelles et al., 2001; Lave and Avouac, 2000]. However, in Bhutan, proposed variable long-term rates of shortening based on thermochronometer integration along balanced cross sections have been estimated to range from as low as ~4 mm/a [Long et al., 2012] to as high as ~76 mm/a [McQuarrie et al., 2014]. We present here three variable deformation velocity scenarios (A, B, C). Velocity A is based on rates proposed by Long et al. [2012] along the Trashigang section with pulses of rapid deformation during MCT motion (31.60 mm/a) and Upper LH duplex formation (37.28-41.28 mm/a) separated by slower periods of deformation for ST activity (14.65 mm/a) and motion along the MBT and MFT (3.99-5.99 mm/a). Velocity B is based on rates estimated by McQuarrie and Ehlers [2013] along the Kuri Chu section ~25 km east of the Trashigang section [Long et al., 2011a]. MCT motion in Velocity B begins at 20 Ma as opposed to 23 Ma in Velocity A and the Lower LH duplex is active from 17-13 Ma. This later age of deformation initiation requires faster motion for the Upper LH duplex (69.42-74.56 mm/a), and other rates in this scenario are comparable to Velocity A. We also test Velocity C for one

flexural model (Split KT, Python Topography), which is similar to Velocity B but calls for relatively slower first motion along the KT (16.67 mm/a) and younger Upper LH deformation. This model allows for understanding how sensitive the modeled ages are to minor changes in age and rate of fault motion. Details for combinations of velocities, heat production values, and flexural models are in Table A-2.

## **4.0 RESULTS**

Discussed below are the results of flexural kinematic modeling and the thermochronometer age prediction model. The first section focuses on the model's first order responses to variations in relative timing of KT motion and sensitivity to topography applied. The second section presents differences in Pecube's predicted cooling ages based on varying heat production, velocity, topography, and kinematics.

### **4.1 FLEXURAL ISOSTASY MODEL**

#### **4.1.1 Isostatic responses to differing KT timing**

A quantitative comparison of the output of all seven flexural models to the published Trashigang cross section [Long et al., 2011a] is presented in Table 1. Among the three different kinematic scenarios, foreland basin thicknesses are deepest with Late KT models and shallowest with Early KT models. Late KT models also produce consistently steeper decollement dips and under-eroded surface geology, which may be attributed to the greater magnitude of late-stage loading in the hinterland of the model. Early KT and Split KT models have average decollement dips shallower than Late KT and generally better matches the surface geology data. However six out of seven models consistently maintain angles steeper than the published section's 4°N dip along

**Table 1** Comparison of the published Trashigang cross section to the outputs of flexural models' final deformed cross sections with varying kinematic sequence and estimated topography.

Cross Section	Foreland Basin Thickness (km)	Decollement Dip	Surface Geology
Long et al. [2011a]	5.6	4°	-
Early KT, Python Topo	4.3	3.8° south of Baxa duplex 6.1° north of Baxa duplex average = 5.0°	over-eroded by 0.5 km at Diuri Fm and Lower LH in ST hanging wall
Early KT, Template Topo	4.5	3.6° south of Baxa duplex 5.2° north of Baxa duplex average = 4.4°	GOOD
Split KT, Python Topo	5.2	4.1° south of Baxa duplex 6.1° north of Baxa duplex average = 5.1°	GOOD
Split KT, Template Topo	4.6	2.9° south of Baxa duplex 4.6° north of Baxa duplex average = 3.75°	over-eroded by 0.3 km in ST hanging wall
Split KT, No Topo	5.1	3.6° south of Baxa duplex 5.5° north of Baxa duplex average = 4.6°	over-eroded by 0.9 km at Diuri Fm over-eroded by 2.3 km in ST hanging wall
Late KT, Python Topo	5.6	4.4° south of Baxa duplex 6.4° north of Baxa duplex average = 5.4°	under-eroded by 0.4 km at Diuri Fm, Lower LH in ST hanging wall, GH synform
Late KT, Template Topo	4.9	4.0° south of Baxa duplex 6.4° north of Baxa duplex average = 5.2°	under-eroded by 1 km at Diuri Fm

footwall flats based on INDEPTH reflection seismology [Hauck et al., 1998], but still within the 4-6° estimated decollement angles for the Main Himalayan Thrust [Ni and Barazangi, 1984; Hauck et al., 1998; Pandey et al., 1999; Mitra et al., 2005; Schulte-Pelkum et al., 2005]. Differences among Early KT and Split KT decollement dips and surface geology are variable, indicating these differences are less a function of kinematics, and appear to be more sensitive to slight variations in crustal density, EET, and topography. The kinematic model that outputs a

best fit to all three of these parameters – foreland basin thickness, decollement dip, and geology exposed at the surface – is Split KT.

#### **4.1.2 Topographic sensitivity in flexural models**

The final topographies differ in their matches to and digressions from observed topography along the Trashigang Section (Figure 10). No Topography obviously does not fit the observed topography and could potentially over-erode the geologic section by 2 km (Table 1, Figure 11). Template topography fits the steep rise in topography seen from ~15 km to ~45 km along the section, from the Diuri Formation outcrop across the Baxa Duplex to the Shumar Thrust. However north of ~45 km, the model topography is at ~1 km greater elevation than observed topography, poorly fitting the northern half of the cross section (Figure 10). Python Topography provides a better fit for the northern half of the section, keeping within ~0.5-1 km of observed topography, and features a local drop in elevation from 77-90 km along section, where a GH zone synform exists (Figure 11) and observed topography decreases. It also captures the first 12 km of the cross section well. The average 2° slope under-predicts elevation by ~0.5-1 km, particularly between 13-55 km, where the average topographic slope of the range is steeper. Overall, Python topography best models actual modern topography along the cross section, and thus has best potential to also fit topography's changes with time as the FTB developed.

The estimated topography is an important component in both isostatic loading and unloading of the modeled section. Because each of the kinematic scenarios influences topographic evolution differently, we will discuss the sensitivity of changing the topography for each kinematic scenario.

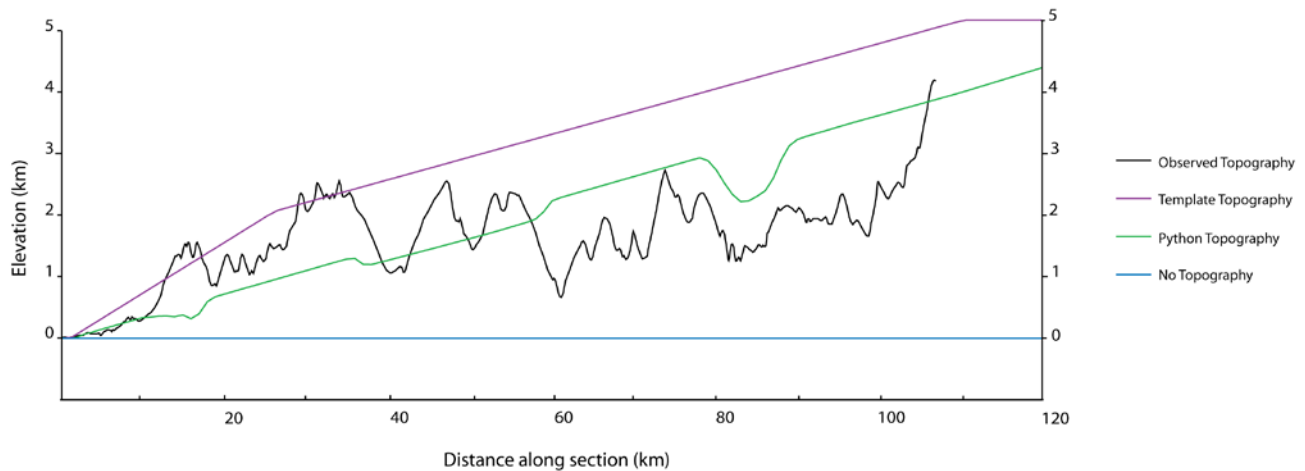
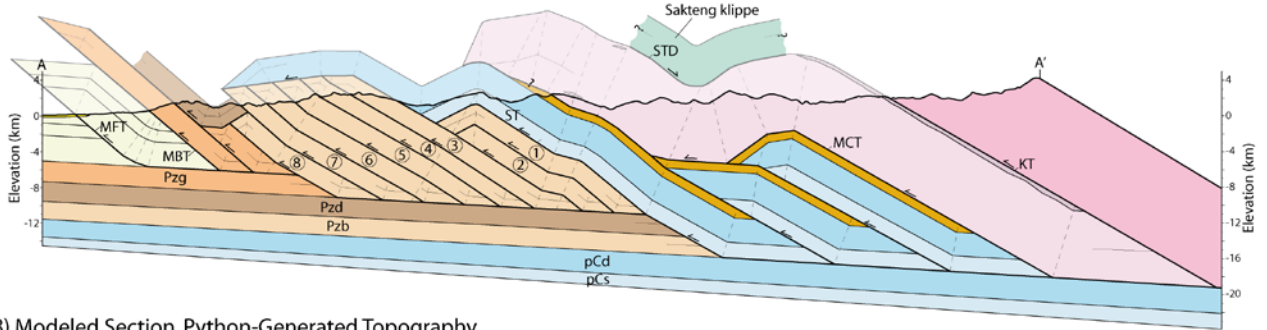


**Figure 10** Modeled topographies of the final deformed cross sections using Split KT compared to observed topography along the Trashigang line of section. Black: Observed Topography, purple: Template Topography, green: Python Topography, blue: No Topography.

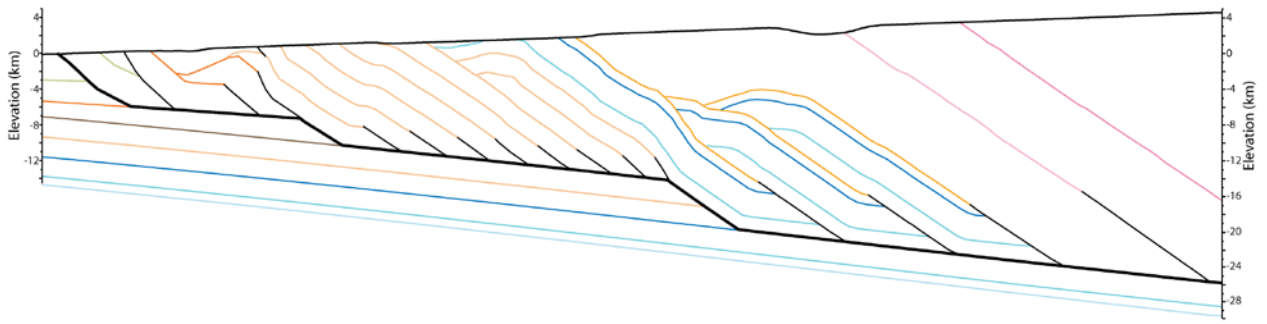
Flexurally modeling the Early KT scenario with Python Topography yielded a surface geology output that is over-eroded by 0.5 km in the Diuri Formation and Lower LH observed along the line of section (Figures 3 and 4) (Table 1). Average decollement dip for this model is  $5.0^\circ$ , and foreland basin depth is 4.3 km. For Template Topography paired with Early KT, surface geology matches the published cross section and the MHT had an average angle of  $4.4^\circ$ . The foreland basin in this model is 0.2 km deeper than the model of Python Topography coupled with Early KT. The opposite trend is seen in the foreland basin depths of Split and Late KT where Python Topography creates deeper foreland basins than Template Topography (Table 1).

We compare the modeled outputs of all three topographic models using the Split KT kinematic scenario in Figure 11. Observed surface geology is matched with Python Topography model, where as the Template Topography model produces a nearly unnoticeable amount of over-erosion (0.3 km) in the hanging wall of the Shumar Thrust. Results of the No Topography

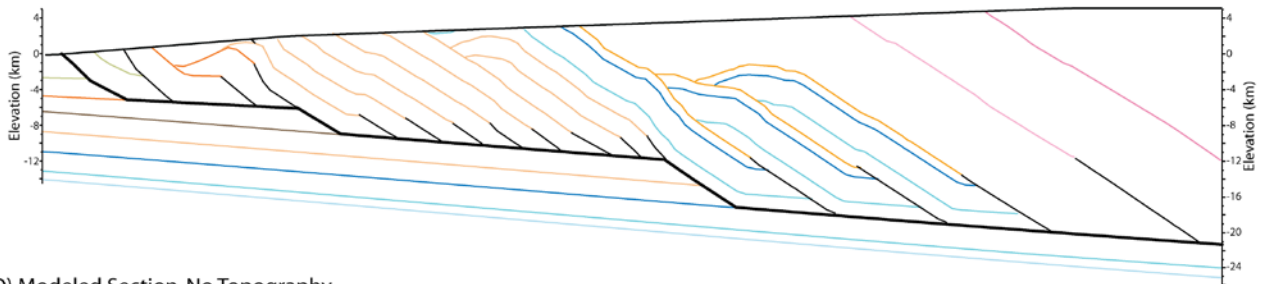
A) Published Trashigang Cross-Section



B) Modeled Section, Python-Generated Topography



C) Modeled Section, Template Topography



D) Modeled Section, No Topography

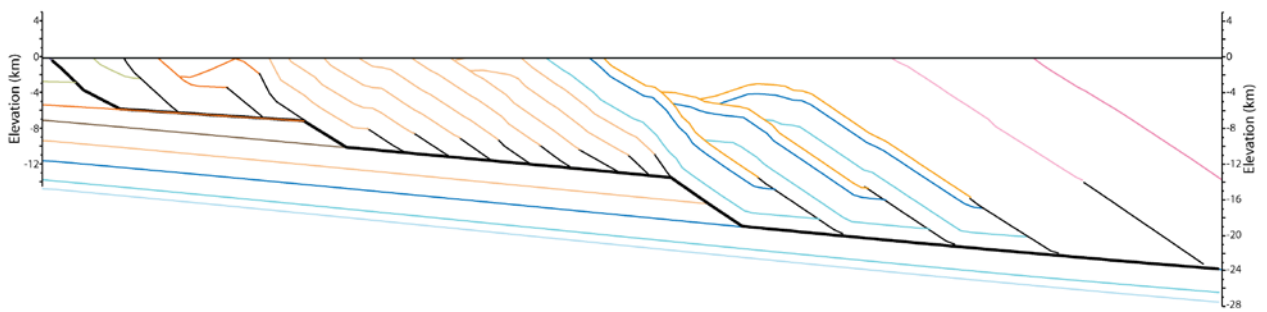


**Figure 11** Published Trashigang cross section (A) compared to flexural model outputs of the Split KT scenario coupled with Python (B), Template (C), and No (D) topography.

model poorly fit observed surface geology. Material in the hanging wall of the ST has been over-eroded by 2.3 km, exposing the underlying Baxa unit at the surface, and 0.9 km of over-erosion occurred along the outcrop of Diuri Formation (Figure 11). Foreland basin thicknesses for Python, Template, and No Topography models are respectively 5.2, 4.6, and 5.1 km. Decollement dips observed for each topographic model are 5.1, 3.75, and 4.6 degrees, respectively (Table 1).

For Late KT kinematic scenario, neither Python nor Template topographies matched observed surface geology (Table 1). This model also produced the steepest MHT angles and deepest foreland basins out of all models tested. The model of Python Topography with Late KT thrust motion preserved 0.4 km too much material across the entire section. Although the Python Topography model produces a decollement dip that is greater than the dip of the published section ( $5.4^\circ$ ), it does attain a match to foreland basin depth (5.6 km). The model using Template Topography with Late KT has a better fit to surface geology with 1 km of localized under-erosion above the Diuri formation exposed south of the Upper LH duplex (Figures 3 and 4). Decollement dip and foreland basin depth for the model using Template Topography and Late KT were  $5.2^\circ$  and 4.9 km. Late KT models had the steepest decollements out of all kinematic models,  $1.2$ - $1.4^\circ$  steeper decollement dips than the published section.

The only observable trend among the topographic models is the decollement dip. Python Topography correlates to steeper MHT angles than Template Topography and No Topography in every scenario. Python topography also consistently results in an average decollement dip steeper than shown in Long et al. [2011a]. This may be attributed to Python's initially shallower topographic angle that misses some of the higher relief of the observed topography (Figure 10), modeling a steeper decollement to accommodate the lower relief when focused on attaining a

best fit to surface geology. Generally shallower dips seen in Template Topography output are the result of an opposite pattern. The steeper Template Topography has a greater area of material above sea level (Figure 10), which models a shallower decollement angle when a best fit to surface geology is prioritized (Figure 11). The overall prioritization of fitting surface geology can consequently compromise each model's fit to other parameters of foreland basin thickness and decollement dip because the area that must fit within the tapered wedge remains constant.

## **4.2 PECUBE PREDICTIVE COOLING AGE MODEL**

### **4.2.1 Heat production sensitivity**

Heat production ( $A_0$ ) values for each thermochronometer are compared for a constant velocity using the Split KT kinematic scenario and the Python Topography (Figure 12). As heat production decreases, Pecube's calculated ages for each thermochronometer increase. This trend is most apparent in AFT, ZHe, and MAr plots from 60-80 km north along the cross section where lower LH rocks are thrust over a ramp in the MHT. The amount by which calculated ages vary with heat production appears to be dependent on the geometry of the decollement. Largest variations are seen where there are ramps in the decollement and where exhumation is greatest. Using a constant velocity, there is no heat production value that will match the data. A best fit for AFT data is observed using a heat production value of  $1.0 \mu\text{W}/\text{m}^3$  (Figure 12a). Matches to ZHe data with  $A_0$  value of  $1.0 \mu\text{W}/\text{m}^3$  only occur at the ends of the section, with a 8.3 Ma cooling age at 14 km and predicted 8-9 Ma ages which overlap with the  $\sim 7.3$  Ma ZHe date at 122 km (Figure 12b). At  $\sim 60$ -70 km along section, using  $2.0 \mu\text{W}/\text{m}^3$  for heat production results in a best fit to

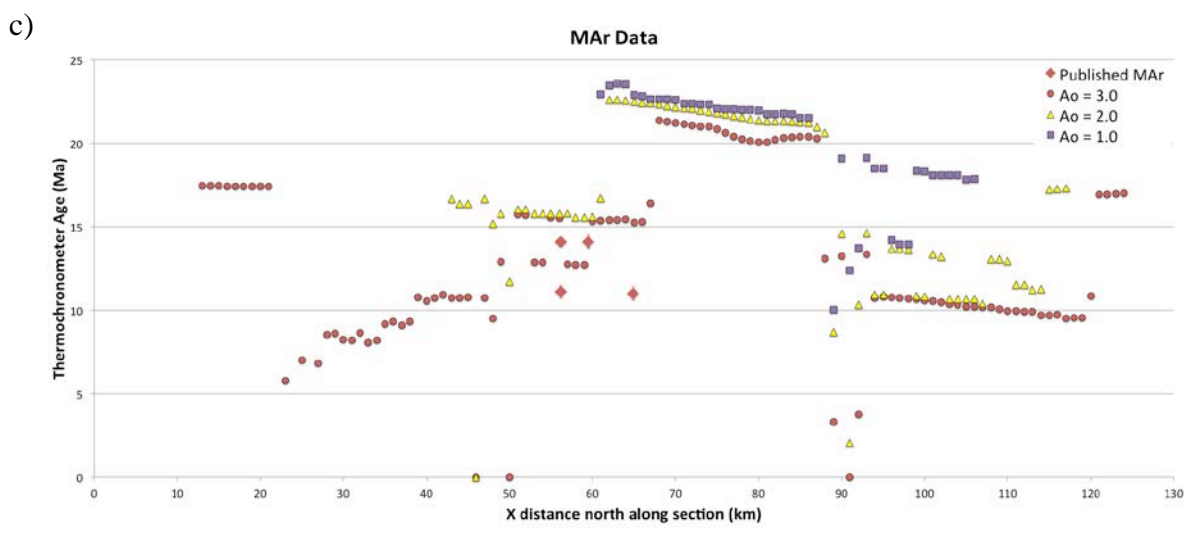
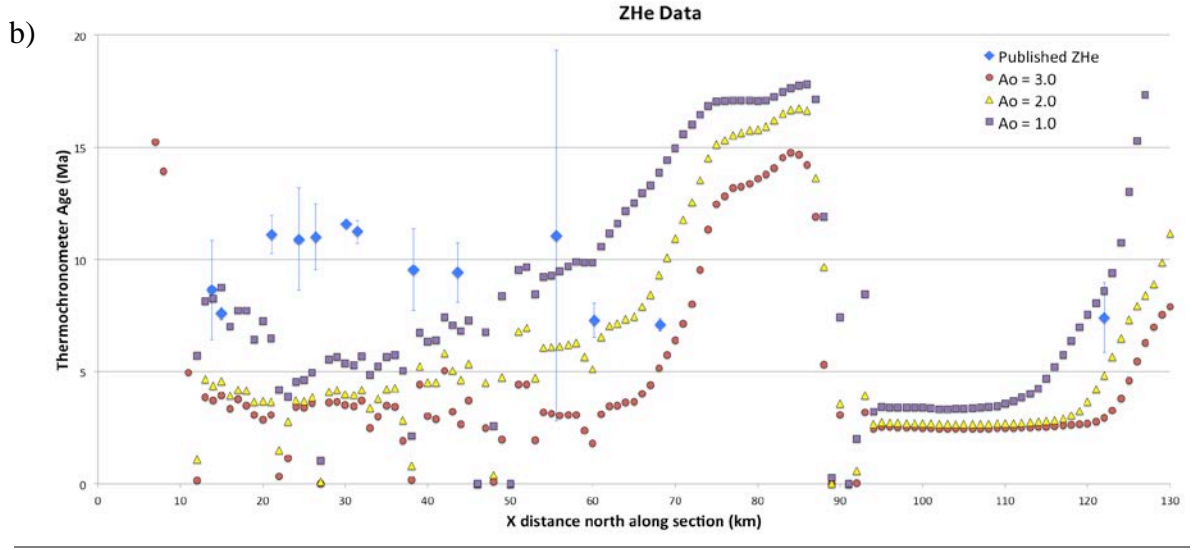
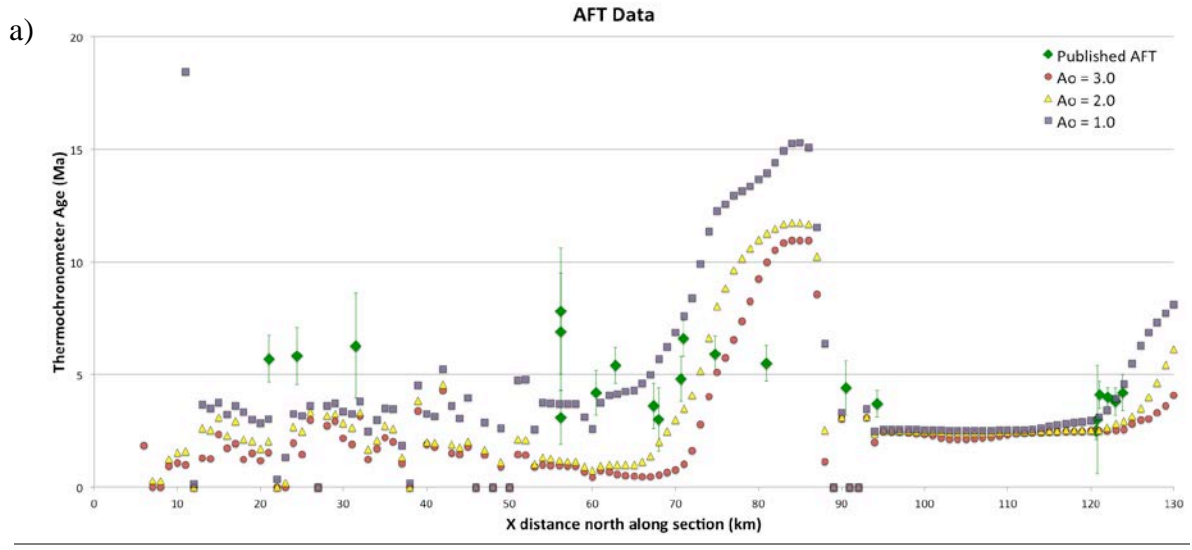


**Figure 12 (previous page)** Pecube output using variable heat production ( $A_0$ ) compared to published AFT (a), ZHe (b), and MAr (c) data.  $A_0$  values in  $\mu\text{W}/\text{m}^3$  are 1.0 (purple square), 2.0 (yellow triangle), and 3.0 (red circle)  $\mu\text{W}/\text{m}^3$ . Other model variables are set as constant velocity, Split KT, Python Topography.

ZHe data. MAr predicted ages provide no match within error to any published data (Figure 12c). Using variable velocities (Section 4.2.2), the predicted age output best matched published data when applying  $2.5 \mu\text{W}/\text{m}^3$  for heat production.

#### **4.2.2 Velocity variation**

A constant rate of deformation does not model cooling age data that match all thermochronometer suites (Figure 12). This requires that deformation rate varies over the time of fold thrust belt development. Pecube's predicted cooling ages and their fit to published cooling ages for Velocity A [Long et al., 2012], Velocity B [McQuarrie and Ehlers, 2013], and Velocity C are discussed below. All variable velocity models presented in this section use a heat production value of  $2.5 \mu\text{W}/\text{m}^3$  and the flexural model of Split KT with Python Topography.

Velocity A is based on rates proposed by Long et al. [2012]. This variable velocity model produces a noticeably better fit than one with a constant deformation rate, and predicts cooling ages that are within error ranges of most published AFT and ZHe data from 12 km to ~70 km along section (Figure 13a). Scatter in predicted AFT cooling ages from ~15-45 km along section range from 10.8-4.2 Ma, and are a function of the second stage of KT motion and a rapid deceleration in deformation rate from 10 Ma to the present (Table A-2). Limited cooling, due to the foreland position of these rocks with respect to young motion on the Kakthang thrust, and

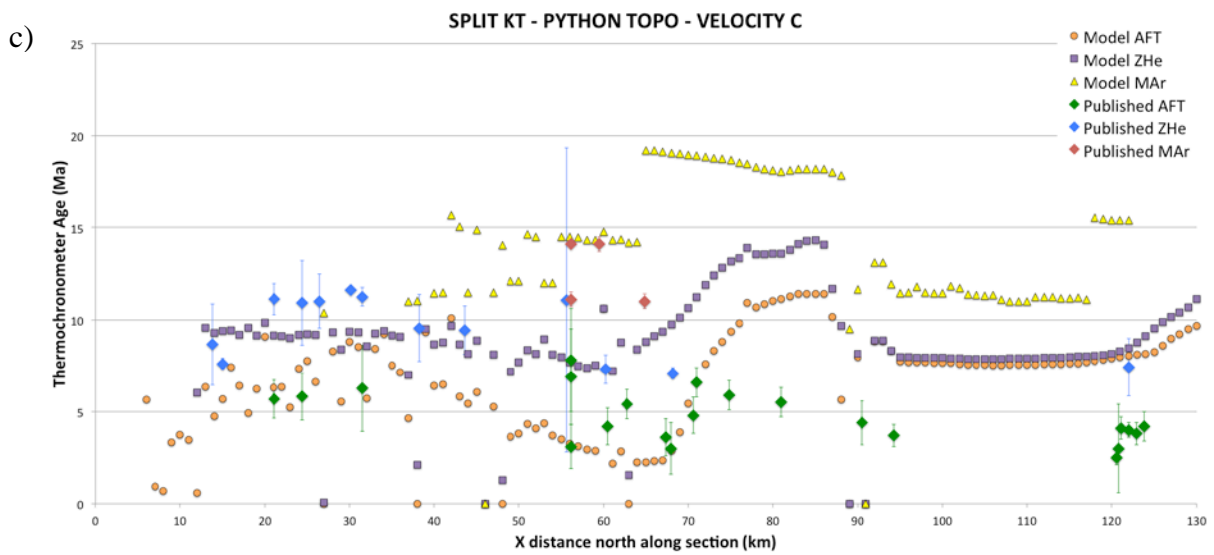
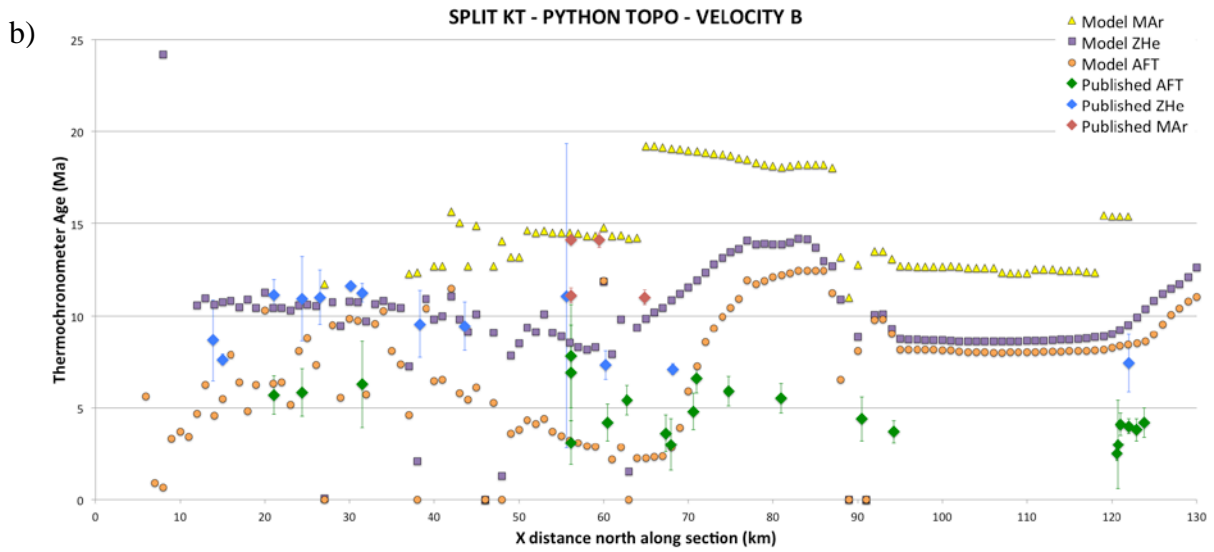
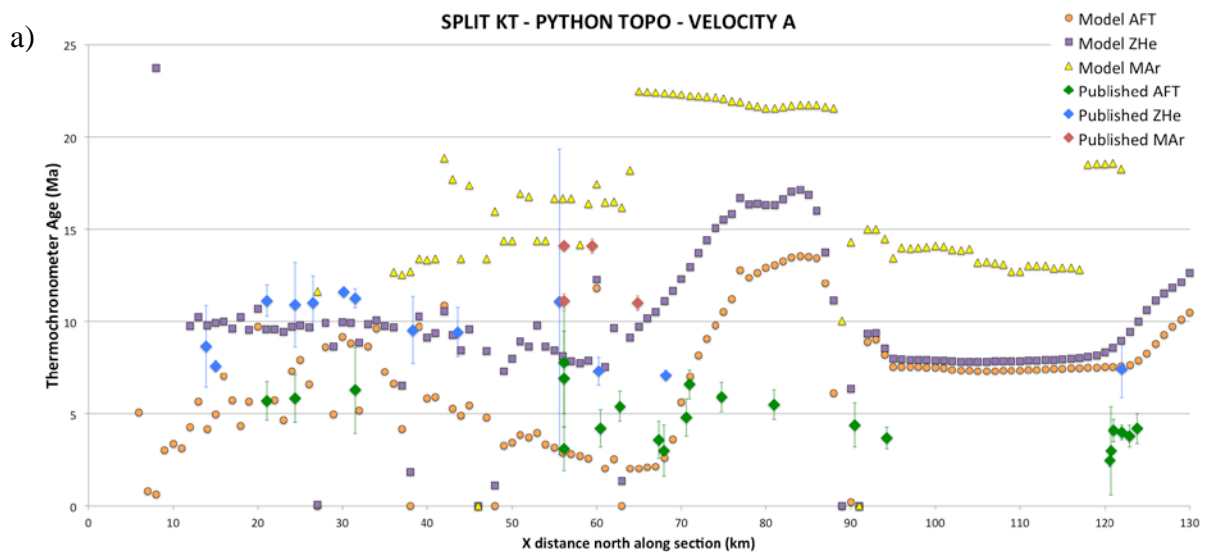


**Figure 13 (previous page)** Pecube output using variable velocities A (a), B (b), and C (c) compared to published AFT, ZHe, and MAr data. Other model variables are set as Split KT, Python Topography, and  $A_0 = 2.5 \mu\text{W}/\text{m}^3$ .

slower shortening rates (5.99 mm/a) created a prolonged timeframe for AFT ages to reset. ZHe ages in this spatial range are noticeably older, between 10 and 9 Ma. These rocks were cooled during the end of Upper LH duplexing and continued to cool and set as they were slowly eroded during KT activity. From ~55-70 km along section, predicted AFT ages fit four out of eight published dates from the GH synform. Predicted AFT ages in the synform systematically increase north of an MHT ramp located at 60-70 km along section; rocks that have not been transported over the ramp are older. Predicted ZHe dates in this area fit one out of only two of the published ages, increasing in age by 64 km along section, resulting in ages too old to fit the published 7.1 Ma cooling date at 68 km. The marked increase in predicted ages is a function of the magnitude of slip and loading on the KT, expanded upon in Section 4.2.4. Predicted MAr dates from ~55 to 65 km produce a three-tier dataset of ages, the youngest of which fits two published data at 14 Ma, with no results that fit the younger ~11 Ma published ages. Modeled MAr ages across the section are set during MCT motion (22.5-21.5 Ma) at 65-90 km, the building of the lower LH duplex (~19-16.5 Ma) at 45-65 km and 120-125 km, and the last 5 km of motion during the first half of KT activity into the first deformed horse building the baxa duplex (14.4-13.0 Ma) at 37-58 km and 90-120 km along section. From ~70 Ma northward, modeled data for AFT and ZHe thermochronometers are too old to fit published data, except for one match within the  $2\sigma$  variation range for a 7.5 Ma published ZHe date at 122 km.

Velocity B based on McQuarrie and Ehlers [2013] applies a rate of Upper LH duplex deformation (74.56 mm/a) that is twice that used in Velocity A, but fits to published data appear

similar to Velocity A (Figure 13b). The most apparent differences are seen with older (11-10 Ma) and more accurately modeled ZHe data from ~20-30 km, and a better fit to the older two published MAr dates due to a younger age for the growth of the Lower LH duplex. MAr data at 11 Ma remains unmatched in this model. Again, most of the predicted AFT and ZHe data from 90 km northward along section are too old; however modeled ages across GH rocks are younger thus a slightly better fit than Velocity A, due to more recent and faster Upper LH duplex initiation. One drawback of this velocity model versus Velocity A is that modeled ZHe ages are too old to fit the northernmost published thermochronometer datum within error. However this model outputs an overall better fit to published data than Velocity A.

In Velocity C results, MAr ages are identical to the output of Velocity B due to identical fault timing for MCT and ST motion (Table A-2) (Figure 13c). The first 25-km motion on the KT in Velocity C (16.67 mm/a) is slower than Velocities A (37.28 mm/a) and B (74.56 mm/a). The modeled MAr data displays a trendline at ~14.3 Ma at 50-65 km along section, within error of one of the published dates, and some younger data in this area at ~12 Ma, within 1.5 km of the southernmost 11.1 Ma MAr datum because of the younger and slower KT. This decelerated KT creates a younger Upper LH duplex (12-9.5 Ma). Younger duplexing in this model results in ZHe ages from 15-45 km that are younger (~9.5-8.5 Ma) than data from velocities A and B. Some of the Velocity C model predicted ZHe ages in this area are younger than the error ranges from 20-30 km. The cooling ages predicted for AFT data from ~10-70 km remain similar to the two other velocities. These cooling ages are set by the end of motion within the Upper LH duplex at ~9.5-11 Ma for all three variable velocities. Younger and closer fitting calculated ZHe and AFT ages are set from 75 to 95 km though still not within the ranges of error for published data. This model does yield the best fit out of Velocities A, B, and C for northernmost ZHe

datum, set by the second stage of motion on the KT, which is younger in this model than in the other velocity scenarios.

### **4.2.3 Topographic sensitivity**

Predicted thermochronometer data for all three topographies modeled with the combination of Velocity B and Split KT are shown in Figure 14. Because the goal for flexural modeling was to match the surface geology and all three sections provided reasonable to very good correlation between modeled and observed surface geology (Figure 11), it is not surprising that the variation in predicted cooling ages for all three topographic scenarios is small (Figure 14). For all three thermochronometers, we notice that modeling with No Topography yields similar or older fitting ages compared to Python Topography, in contrast to expectations that the generally over-eroded final No Topography model would produce younger cooling ages than the other topographies. Increased density coupled with No Topography thus may have caused a different flexural history and influenced cooling ages differently than the other topographies. Although variations are subtle, the model with No Topography produces the poorest fits out of the three topographies except in the case of MAr, where fit is approximately the same as the Python and Template Topography models (Figure 14c).

Modeling with Template Topography also results in predicted ages similar to Python Topography but outputs more scattered data across all chronometers. This is most important in the output of AFT data (Figure 14a). Modeled AFT ages using Template Topography include distinctly younger cooling data (~4-7 Ma) intermittently spaced along most of the cross section (5-85 km). These younger ages are a function of the modeled topography lacking net subsidence when the model is flexurally loaded during the second stage out-of-sequence thrusting. In

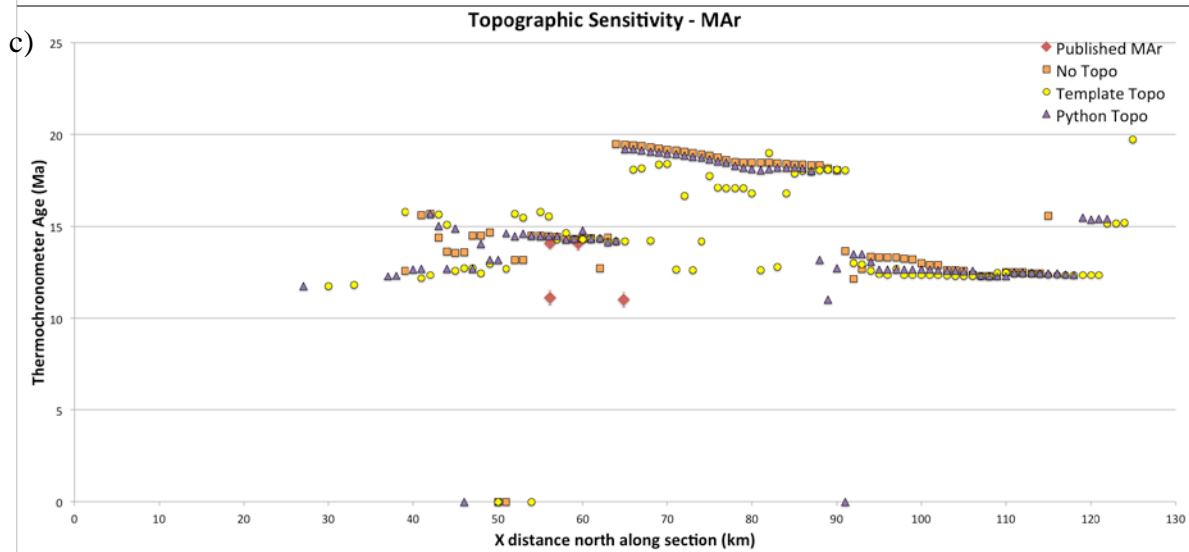
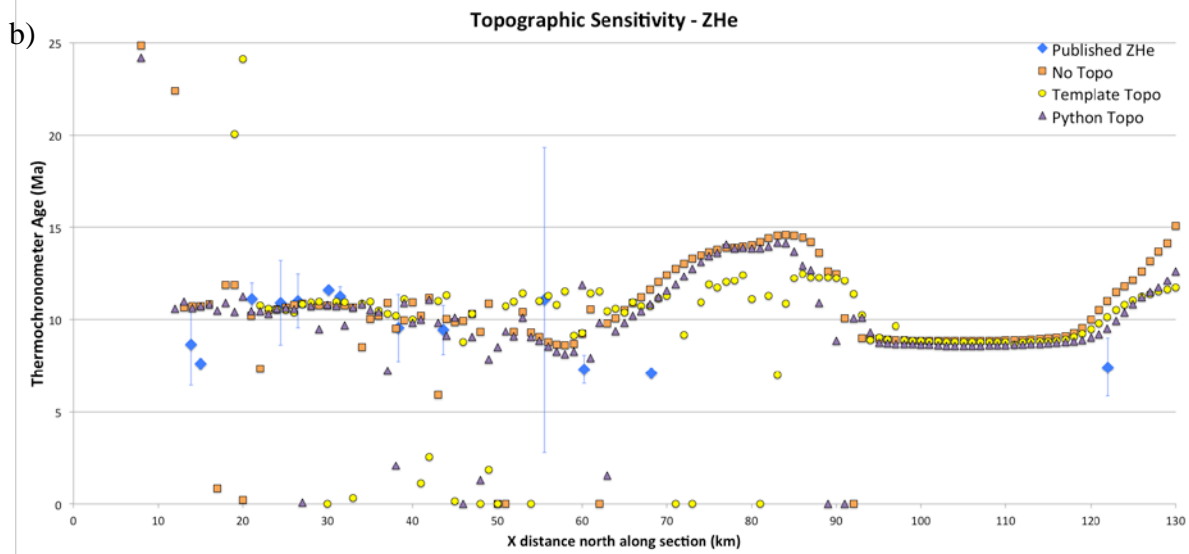
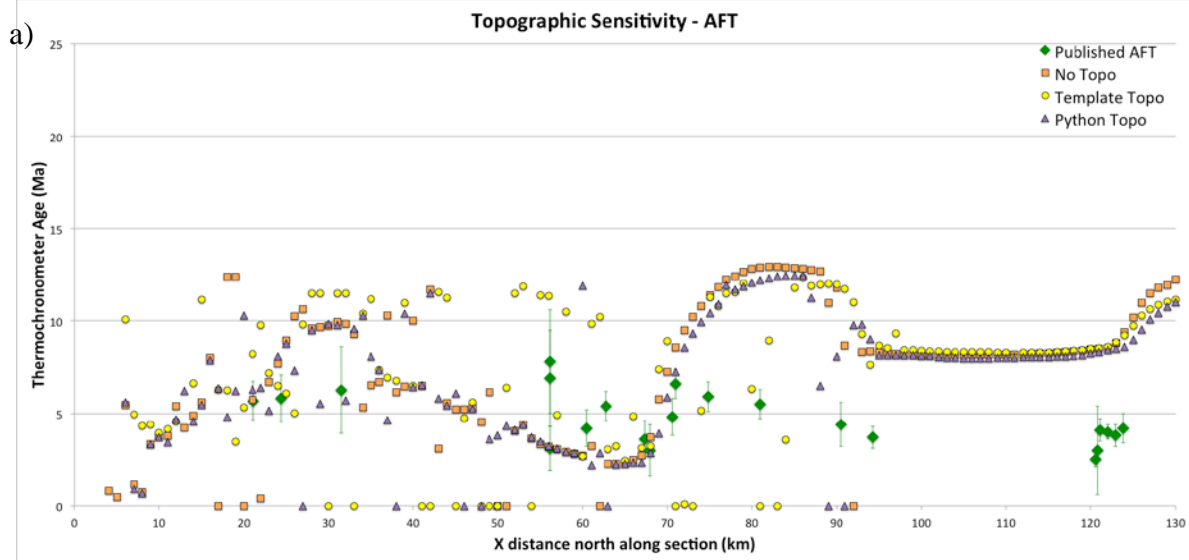


**Figure 14 (previous page)** Pecube output using variable topography models compared to published AFT (a), ZHe (b), and MAr (c) data. Topographies used are No Topography (orange square), Template Topography, (yellow circle), and Python Topography (purple triangle). Other model variables are set as Split KT, Velocity B, and  $Ao = 2.5 \mu\text{W}/\text{m}^3$ .

addition, Python Topography models ongoing erosion and mineral cooling in the south during out-of-sequence motion while Template Topography does not. This ongoing erosion facilitates younger AFT ages between 20-60 km for Python Topography than Template Topography. These trends highlight that the misfit in ages between 70 and 95 km may be a function of how out-of-sequence faulting is flexurally accommodated (Figure 8), and that this flexural accommodation affects the predicted cooling history. These fits also suggest that the load modeled for the KT may be too high, and the amount of motion on the KT may be too large.

#### **4.2.4 Kinematic variation**

Thermochronometer output for each of the three kinematic scenarios coupled with Python Topography are compared in Figure 15 using Velocity B. Modeled fits to MAr data appear to be unaffected by varying timing of out-of-sequence thrusting. However the other two chronometers do differ based on kinematic scenario. The gap in ZHe and AFT ages observed at 20-30 km along section is only matched within error of both chronometer datasets using Split KT. Models using Early KT and Late KT scenarios output fits to AFT ages in this area, but ZHe ages are modeled too young in both cases. This indicates that out-of-sequence motion is required after the entire Baxa duplex has been deformed. From ~30-60 km along section, data appear similar. ZHe ages using the Early KT model are noticeably younger by ~3 myr at ~55 km along section. North of 60 km, AFT and ZHe model output using Early KT is continuously younger than the

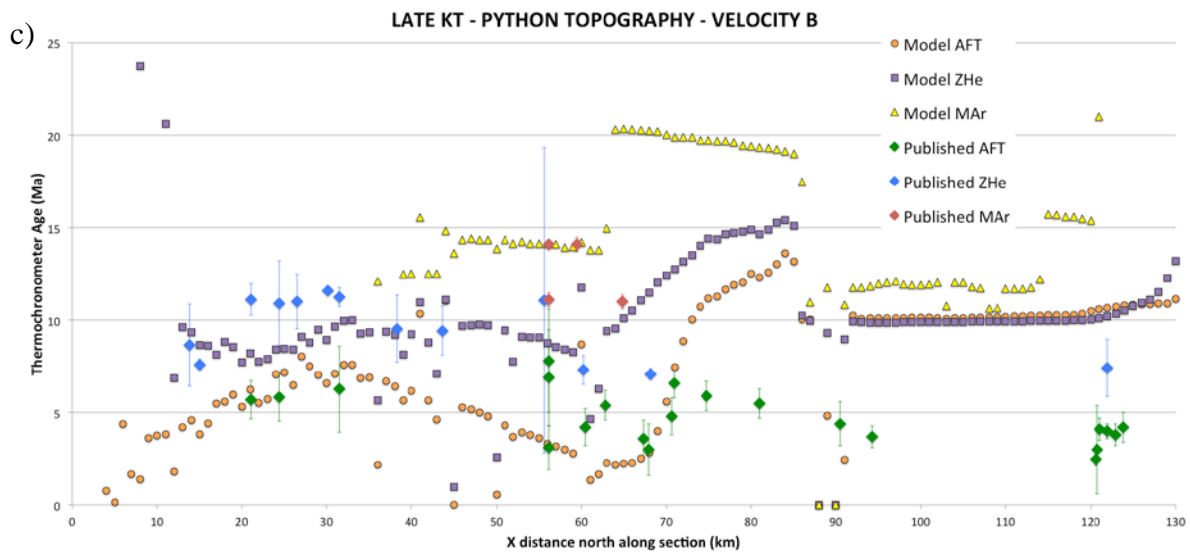
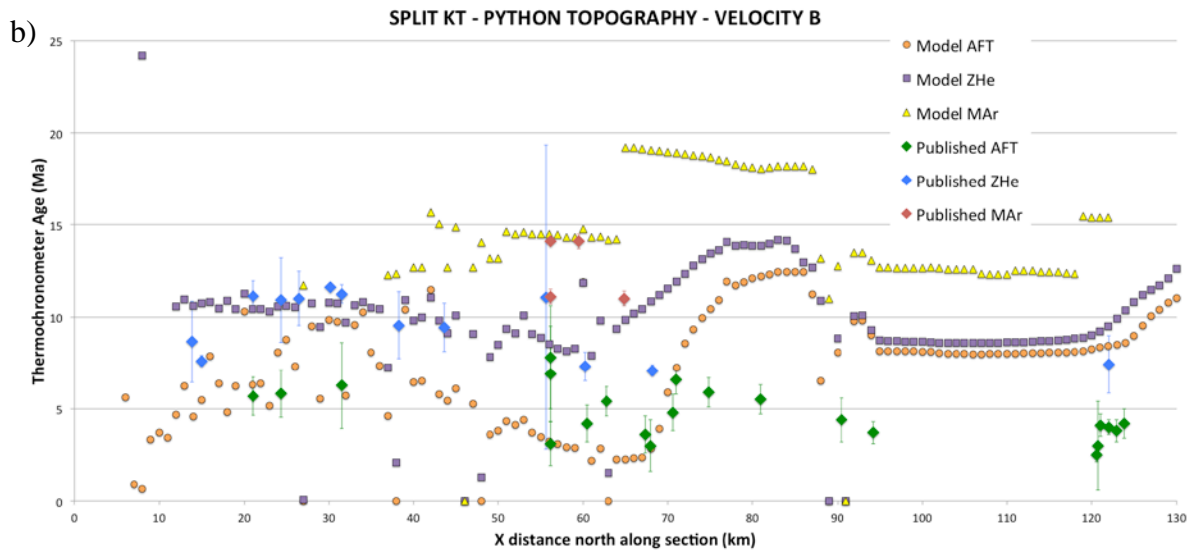
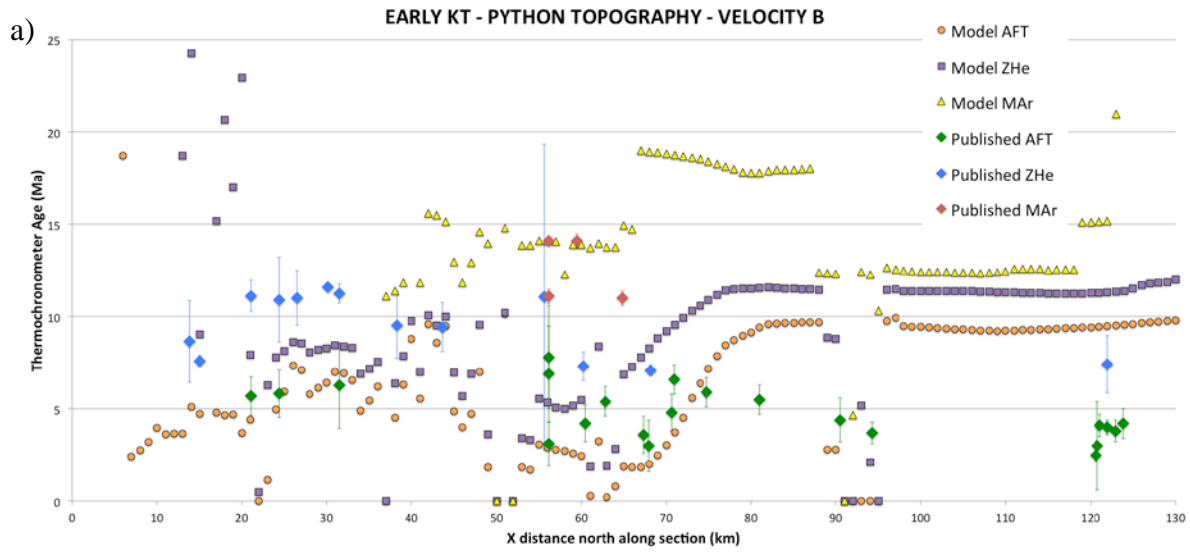


**Figure 15 (previous page)** Pecube output using models with Early KT (a), Split KT (b), and Late KT (c) compared to published AFT, ZHe, and MAr data. Other model variables are set as Python Topography, Velocity B, and  $A_0 = 2.5 \mu\text{W}/\text{m}^3$ .

other models, more closely fitting the young 4-6 Ma ages observed from ~70-90 km along section but still not within error (Figure 15a). The Early KT shows the youngest ages in this region because it allows for the most exhumation after KT motion than the other models, as well as younger active uplift and heightened erosion associated with the Baxa duplex and transport of these northern rocks over a Lower LH ramp (Figure 7B-D) when these ages are set. These results suggest that KT motion is also required prior to deformation of the Baxa group. This interpretation is strengthened by the output of Young KT (Figure 15c), which models the earliest onset of Baxa duplexing and outputs the oldest and worst fitting AFT data across the GH zone out of these three kinematic scenarios. The amplitude of this concave-downward trend of older ages modeled from 90-70 km along section is thus related to the magnitude and relative timing of out-of-sequence KT motion. Combining these results with those of the topographic sensitivity tests, we affirm that modeled cooling ages in this area are a function of flexural accommodation, topographic evolution, and age of out-of-sequence thrusting.

## 5.0 DISCUSSION

### 5.1 EVALUATING AGREEMENT BETWEEN MODELED AND PUBLISHED DATA

Out of all flexural model variations reported in Results (Section 4), we find a best fit to published cooling ages using Split KT with Python Topography (Figure 13). Variable velocity tests conclude that deformation rates proposed by McQuarrie and Ehlers [2013] (Velocity B) provided best fits to published cooling ages. However our results are non-unique, as some of the other flexural models tested can produce trends in calculated cooling ages that still reasonably fit observed thermochronologic data.

The flexural model of Split KT with Favorite Topography, for instance, does adequately reproduce a significant number of published cooling ages when pared with Velocity B and  $2.5 \mu\text{W}/\text{m}^3$  heat production (Figure 16). Predicted MAr ages fit well to published MAr ages at 14 Ma. Modeled ZHe data also fit published ages well from 20-45 km along section, but ZHe ages are not reset from 0-20 km and poorly fit the observed 7-8 Ma ages at ~14 km along section. Between 50 and 90 km, ZHe output are too old, (12.5-10 Ma), only fitting one out of three of the published ages across this area (7.09, 7.30, 11.07 Ma). Scattered AFT output acceptably fits two out of three published data from ~20-30 km, and farther along section between 55 and 95 km the younger intermittent ages (2-6 Ma) also model 6 out of 13 published AFT ages (2-6 Ma), providing a better fit in this region than the Python Topography model. So while best fitting

datasets tend to be output when modeling with Split KT and Python Topography, this model using Template Topography can still generate similar data trends and may output a better fit with modified ages of fault motion.

The poor fit to the young AFT ages found in the GH rocks at ~70-95 km among models tested in this study indicates that refinement is needed in either cross section geometry, or flexural accommodation and topographic prediction during out-of-sequence thrusting, to better match the thermochronologic data.

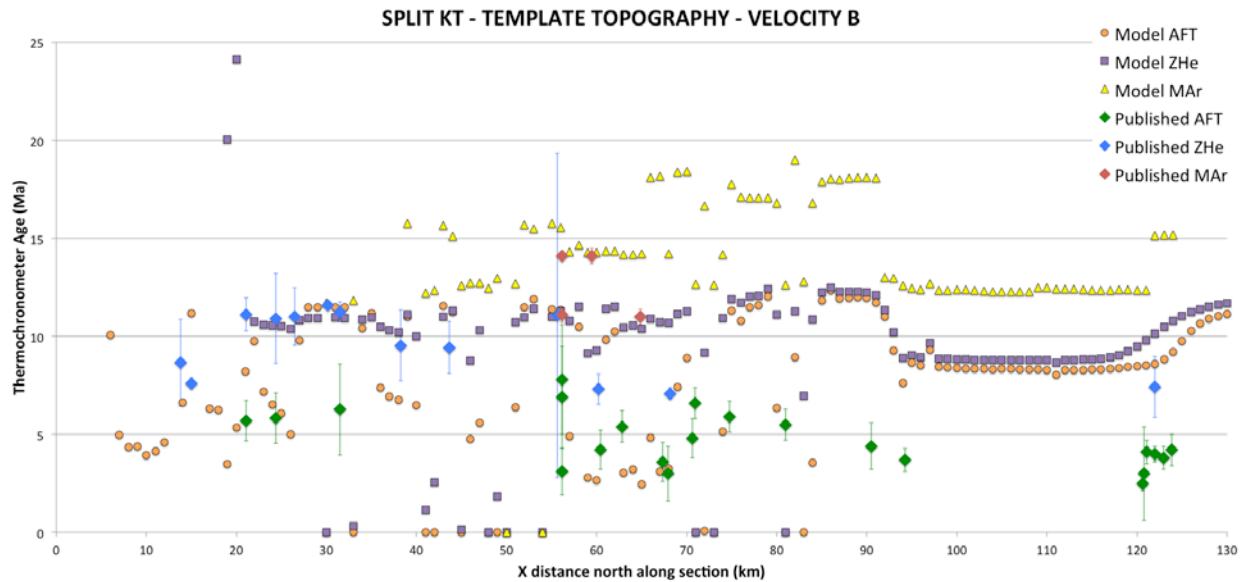


**Figure 16** Pecube output using model with Split KT, Template Topography, Velocity B, and  $A_0 = 2.5 \mu\text{W}/\text{m}^3$  compared to published AFT, ZHe, and MAr data.

### 5.1.1 Possible geometric solutions

Because geometry of the cross section has a first order control on ages [McQuarrie and Ehlers, 2013], a solution to the difference in predicted and modeled ages may be adjusting ramp location. In most of the models tested, AFT ages in Greater Himalayan rocks are set by motion

over the last ramp they encounter. In the current cross section geometry, the final ramps over which GH rocks are thrust are (1) from ~55-70 km along section, the footwall cutoff of Baxa and Diuri units during MFT motion, which can be successfully modeled; and (2) from ~70-95 km, the footwall cutoff of the Daling formation during Baxa Duplexing (Figure 7 B-D). This latter ramp is setting AFT ages too early (e.g., ~10-13 Ma in Figure 13). Simply moving the footwall ramp of Baxa and Diuri units farther north to reset all of the AFT ages in GH rocks would not solve this problem though. A single active ramp in this location would produce AFT data of ~2-3 Ma, such as the young measured ages at ~60 km (Figure 13). These data would be younger than the observed ~4-6 Ma ages between 70-95 km. The predicted ages would also become older south of the ramp, producing poorer fits to the currently well-constrained data at 55-70 km. A possible solution may be to break up the single footwall ramp through the Baxa and Diuri, to two offset ramps. The Diuri ramp would remain in its current location where the youngest AFT ages are set, and the Baxa ramp would be shifted farther north to the location of the slightly older (~4-6 Ma) data.

### **5.1.2 Possible flexural and topographic solutions**

Another solution would re-evaluate how the flexural model accounts for out-of-sequence thrusting with respect to magnitude, sequence, and isostatic loading of the Kakhtang Thrust as well as how topography responds over this time. Comparing Pecube output for varying kinematic scenario, the youngest AFT ages at 70-95 km along section are modeled with Early KT, though these ages are still a poor fit to the 4-6 Ma observed data in this area (Figure 15a). Re-evaluating the partitioning of slip in the Split KT scenario, such as increasing the amount of slip in the first stage of KT motion, may produce younger data. However because the model of Old KT with

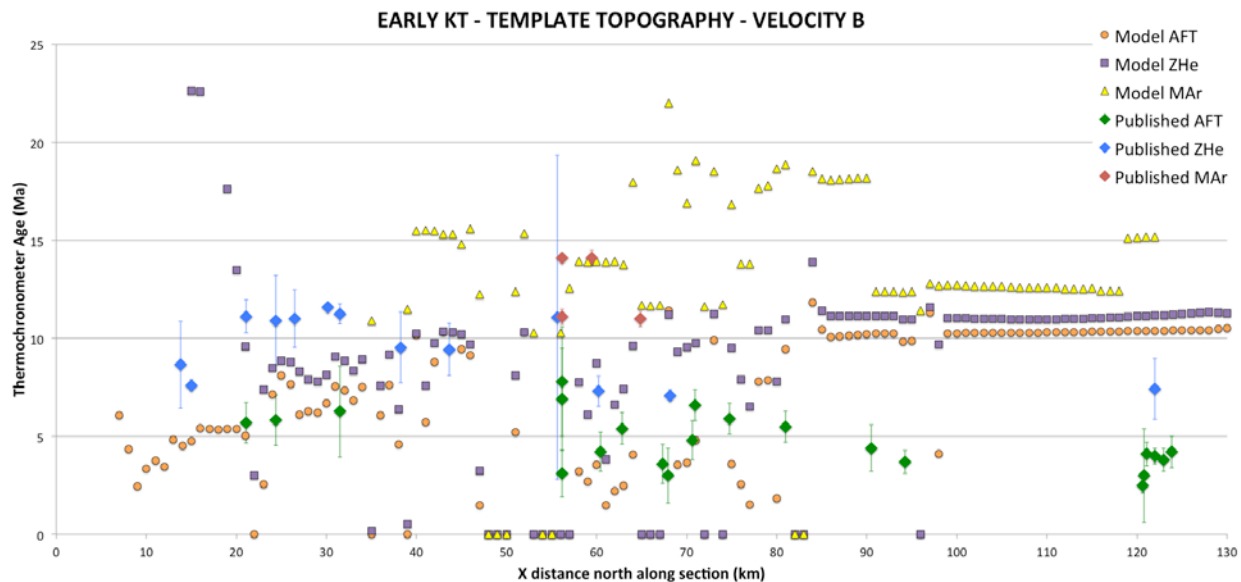


**Figure 17** Pecube output using model with Early KT, Template Topography, Velocity B, and  $A_0 = 2.5 \mu\text{W/m}^3$  compared to published AFT, ZHe, and MAr data.

Python Topography still does not adequately fit the young AFT data observed in the Greater Himalaya, adjusting topography, and the flexural load associated with topography is necessary to yield a better fit to the predicted AFT cooling ages. This is best seen in how modeling with Template Topography, which is not adjusted for the flexural load, results in younger AFT data that more closely match the observed 4-6 Ma AFT ages at 70-95 km. This trend is observable in the model coupling Template Topography with Split KT (Figure 16) and even more apparent with Early KT (Figure 17), which models AFT data in the Greater Himalaya that are too young to fit published ages at ~70-80 km along section. Thus a solution using a modified Python Topography and a Split KT scenario with most of the KT motion being older may generate a good fit to data. The topographic angle in the python script can be altered to produce less topographic uplift associated with KT motion. With less topographic relief, less erosion and

subsidence would occur over this time window, which will alter the AFT cooling age in GH rocks and may model a better fitting pattern of young AFT ages from 70-95 km along section. Therefore, in a new flexural model, a combination of more motion in the first stage of KT motion along with less topography relief on the KT may output a better match the observed ages across the GH.

## **5.2 DEFORMATION TIMING AND VELOCITY RANGES FITTING PUBLISHED DATA**

Based on the outputs of the variable velocity models presented here, we see that motion along specific structures produce a resulting pattern in cooling ages. When the age of the structure is changed, the predicted cooling ages set by motion on or over that structure correspondingly change. Thus we can analyze the required timing necessary for model ages to best fit the published thermochronometer data. Age of motion on the MCT does not change how modeled ages fit published data along the section. Therefore initial MCT motion could occur either at ~23 Ma [Long et al., 2012] or ~ 20 Ma [McQuarrie and Ehlers, 2013]. Modeled MAr data in Velocities B and C offer closest matches the published ~14 Ma ages (Figure 13), set during formation of the Lower LH duplex, which is completed in these two models at 13.5 Ma (Table A-2). Most MAr data along the strike of the ages used in this study, east of the Trashigang section, display ages from ~9-13 Ma [Long et al., 2012], so 14 Ma ages observed in our cross section may be at the upper limit of the MAr cooling window in this area. Adequately modeling the younger data that better matches other ages at 11 Ma requires very rapid deformation during Upper LH duplexing (>100 mm/a) to maintain fits for the ~9.5-11 Ma ZHe ages measured in the

Upper LH zone (Figures 3 and 5). These ZHe ages are influenced by structural uplift and associated exhumation at the end of Upper LH duplexing and continue to cool during first 10 km of the second stage of KT motion. Upper LH duplexing ends sometime between 11.5 and 9.5 Ma based on the fits of all three of our velocity tests. Reasonable fits to AFT data across velocities A, B, and C, in the Upper LH are set by continued cooling through KT motion and active uplift at the beginning of MBT activity at ~7.5-6.5 Ma. Initiation of motion on the MBT may be as recent as 5.5 Ma and still fit the data within the margin of error for published ages. Final motion on MBT and MFT facilitates the AFT cooling ages observed ~55-70 km along section, and velocities A, B, and C all fit the data (within error) with initiation of motion on the MFT between 4 and 2 Ma.

We can place reasonable limits on rates of deformation in the eastern Himalayan fold-thrust belt of Bhutan by evaluating the timing of fault motion in models that output predicted cooling ages comparable to published thermochronometer data. With MCT activity proposed from c. 23-20 Ma to c. 21-17 Ma [Long et al., 2012; McQuarrie et al., 2014], slip can be applied at a minimum rate of 10.53 mm/a, with no known maximum rate of shortening. MCT slip rates tested in this study ranged from 21.7 to 31.6 mm/a. The success of modeling MAr data is restricted to velocity models B and C (Figure 13), and thus motion along the Shumar Thrust is constrained between ~17 and 13.5 Ma at a shortening rate of ~25 mm/a. Modeled rates for the first 25 km of KT motion ranged from 16.7 mm/a (13.5-12.0 Ma) to 74.6 mm/a (13.5-13.2 Ma) with good fits for both sets, indicating a wide range possible velocities for this period of deformation. Deformation rates during Upper LH duplexing that modeled fits to published ages ranged from 64.6 mm/a (Velocity C) to 74.6 mm/a (Velocity B). Based on calculations of maximum and minimum ages that could yield a fit to cooling data, possible rates could be as low

as ~37 mm/a (~14-10 Ma) or greater than 100 mm/a. For our best fitting Split KT kinematic scenario, rapid deceleration for the second 20-km pulse of KT activity is required, which can start from 11.0-9.5 Ma and end at 7.5-6.5 Ma, giving possible rates ranging from ~10-4 mm/a. Rates of motion along the MBT can range from 10.6-4.8 mm/a based on modeled cooling trends, initiating at 7.5-6.5 Ma and ending by 4-2 Ma. MFT deformation rates that output matches to published AFT data ranged from 6.7-3.3 mm/a. This relatively slow velocity implies very recent 2-0 Ma acceleration in motion along the MFT to the observed modern convergence rate of ~15-25 mm/a [Bilham et al., 1997; Larson et al., 1999; Banerjee and Burgmann, 2002; Zhang et al., 2004; Bettinelli et al., 2006; Banerjee et al., 2008].

### **5.3 COMPARISON TO OTHER THERMAL-KINEMATIC MODELING ALONG THE TRASHIGANG SECTION**

Results from this study indicate that variable velocity over time is required to accurately model cooling rates by using a sequential, kinematically and flexurally deformed cross section model as input in forward model Pecube. The importance of variable velocity is true even when adjusting for a variety of other parameters that influence cooling ages (heat production, kinematic order, topography) while holding section geometry constant. Coutand et al. [2014] used Pecube to invert a suite of thermochronometer data (ZFT, ZHe, AFT, ZHe) along the same line of section but held the rate of convergence between India and Tibet constant while allowing for variation in section geometry, heat production, and temporal changes in rates of underthrusting and overthrusting. Because of the differences in what has been held constant as well as the thermochronometers that are modeled and the timeframe over which the study is focused (~23

Ma vs. 10 Ma), we cannot directly compare quantitative results between studies. However some general findings by Coutand et al. [2014] are similar to our results. In eastern Bhutan their study concluded that a rapid deceleration in exhumation rates and overthrusting rates is needed at 6 Ma. Similar trends in deformation rates can be seen in this study, with a slowing of rates at 10 and 11 Ma for velocities A and B, while for velocity C a deceleration is modeled at 9.5 and 7.3 Ma. Coutand et al. [2014] also conclude that their results are more compatible with tectonically driven erosion processes than climate-driven erosion, particularly controlled by fault geometry and kinematics, with which this study is in agreement.

## 6.0 CONCLUSIONS

Our flexural models of sequential deformation of the Trashigang cross section with varying kinematic sequences and topographies, and their use in thermal-kinematic modeling of thermochronologic data in Eastern Bhutan, allow for the following conclusions:

1. Applying flexural isostasy to kinematic models successfully reproduces a deformed cross section with evolving foreland basin, decollement, and surface geology. With small amounts of slip applied in each flexural step, deformational and exhumational histories of fold-thrust belts along with depositional histories of associated foreland basins can be modeled at high spatial and temporal resolution.

2. Varying kinematic timing of faulting, particularly for the out-of-sequence Kakhtang Thrust in this study, results in a different flexural model output. Variations to topography also change model output based on the steepness of topography used and how each topography accounts for flexural loading.

3. Forward thermal-kinematic models of cooling ages, using flexural models as input, reveal that predicted ages are sensitive to (1) variable rates of deformation, (2) modeled topography's ability to account for structural uplift and flexural loading, (3) kinematic timing of fault motion, and (4) cross section geometry.

4. Models maintaining constant deformation rate across the entire Himalayan fold-thrust belt can not adequately predict cooling ages matching published AFT, ZHe, and MAr data. Best

fits to the suite of cooling ages tested had deformation velocities that varied from 73 mm/a to as low as 4 mm/a during fold-thrust belt development.

5. We suggest zones of data that cannot be adequately modeled have cooling ages influenced by (1) a decollement geometry that differs from the tested cross section, particularly concerning the location of footwall ramps in the Lesser Himalaya, and/or (2) how out-of-sequence motion along the Kakhtang Thrust is accommodated in the flexural model.

6. This workflow of coupling a high-resolution flexural model of a balanced cross section with thermal-kinematic model Pecube can be used to quantify magnitude, timing, and rates of deformation in compressional settings.

## **APPENDIX A**

### **SUPPLEMENTARY INFORMATION**

Included in this section are supplementary data tables detailing published thermochronologic data used in this study (Table A-1) and combinations of flexural and thermal-kinematic model inputs tested in Pecube (Table A-2).

**Table A-1** Thermochronometer sample locations, original studies, and cooling ages used in this study. Note that listed ZHe ages are based on the mean reported age among all aliquots for each sample, and include a variability range instead of analytical error. Latitude and longitude of samples from Stüwe and Foster [2001] were estimated using WGS84 datum.

Sample	Study	Unit	Elevation	Latitude (°N)	Longitude (°E)	Map Distance Along Section (km)	Central AFT Age (Ma)	2 $\sigma$ Analytical Error (Ma)	Mean ZHe Age (Ma)	2 $\sigma$ Variability Range (Ma)	Reported AFT Age (Ma)	2 $\sigma$ Analytical Error (Ma)
BU07%3	Long,et,al.,[2012]	Pzg	655	91.48011	26.86572	13.84			8.65	2.22		
BU07%4	Long,et,al.,[2012]	Pzd	700	91.48028	26.87497	14.99			7.61	0.28		
BU07%3	Long,et,al.,[2012]	Pzd	1710	91.54794	26.93311	21.08	5.69	1.04	11.12	0.85		
BU07%5	Long,et,al.,[2012]	Pzb	1580	91.54761	26.95992	24.41	5.82	1.28	10.91	2.29		
BU07%6	Long,et,al.,[2012]	Pzb	1785	91.53083	26.97442	26.46			11.00	1.47		
NBH%8	Long,et,al.,[2012]	Pzb	1815	91.52072	27.01200	30.14			11.60	0.03		
BU07%7	Long,et,al.,[2012]	Pzb	2385	91.50142	27.02675	31.48	6.27	2.34	11.25	0.50		
BU07%2	Long,et,al.,[2012]	Pzb	2165	91.52089	27.08486	38.28			9.54	1.82		
BU07%3B	Long,et,al.,[2012]	Pcd	2315	91.56708	27.13450	43.61			9.43	1.33		
BU07%5	Long,et,al.,[2012]	Pzj	2350	91.52122	27.24222	55.60			11.07	8.27		
BH53	Grujic,et,al.,[2006]	GHlo	2405	91.548083	27.237361	56.15	6.9	2.6				
BH52	Grujic,et,al.,[2006]	GHlo	2350	91.554667	27.236056	56.15	7.8	2.8				
8	Stuwe,&Foster,[2001]*	GHlo	2540	91.53157	27.24116	56.15					14.1	0.2
9	Stuwe,&Foster,[2001]*	GHlo	2480	91.52660	27.24549	56.15	3.1	1.2			11.1	0.4
11	Stuwe,&Foster,[2001]*	GHlo	1750	91.53157	27.24116	59.48					14.1	0.4
BH%7	Long,et,al.,[2012]	Pcd	605	91.44656	27.27869	60.22			7.30	0.77		
BH60	Grujic,et,al.,[2006]	Pzj	795	91.480667	27.282361	60.46	4.2	1.0				
BH61	Grujic,et,al.,[2006]	GHlo	780	91.491000	27.303417	62.80	5.4	0.8				
12	Stuwe,&Foster,[2001]*	GHlo	1060	91.54378	27.32288	64.87					11.0	0.4
BH90	Grujic,et,al.,[2006]	GHlo	910	91.574528	27.344972	67.32	3.6	1.0				
BH64	Grujic,et,al.,[2006]	GHlo	825	91.554472	27.350056	67.94	3.0	1.4				
BH%8	Long,et,al.,[2012]	Pzc	1000	91.63897	27.35144	68.19			7.09	0.28		
BH324	Grujic,et,al.,[2006]	GHlo	1995	91.59683	27.374361	70.61	4.8	1.0				
BH94	Grujic,et,al.,[2006]	Pzc	2050	91.599833	27.375333	70.94	6.6	0.8				
BH100	Grujic,et,al.,[2006]	GHlo	905	91.563722	27.411389	74.77	5.9	0.8				
BH72	Grujic,et,al.,[2006]	GHlo	1420	91.554722	27.465000	80.96	5.5	0.8				
BH66	Grujic,et,al.,[2006]	GHlo	930	91.561139	27.551361	90.50	4.4	1.2				
BH70	Grujic,et,al.,[2006]	GHlo	1760	91.499528	27.584167	94.27	3.7	0.6				
BH%63	Coutand,et,al.,[2014]	GHh	3610	91.37263	27.96956	120.64	2.5	0.4				
BH%51	Coutand,et,al.,[2014]	GHh	3870	91.30357	27.97318	120.79	3.0	2.4				
BH%52	Coutand,et,al.,[2014]	GHh	3880	91.29016	27.97416	121.10	4.1	0.6				
BH%57	Coutand,et,al.,[2014]	GHh	4085	91.29827	27.98563	122.01	4.0	0.4	7.42	1.56		
BH%55	Coutand,et,al.,[2014]	GHh	4275	91.2987	27.99005	122.93	3.8	0.6				
BH%62	Coutand,et,al.,[2014]	GHh	4300	91.29901	27.99750	123.85	4.2	0.8				

**Table A-2** Combinations of flexural models' out-of-sequence KT placement and topography, velocity, and heat production (Ao) variations used as Pecube input.

a) Early KT

VELOCITY: TOPOGRAPHY: Ao ( $\mu\text{W}/\text{m}^3$ ):		CONSTANT PYTHON, TEMPLATE 2.0, 2.5, 3.0		VELOCITY A PYTHON, TEMPLATE 2.25, 2.5, 2.75, 3.0		VELOCITY B PYTHON, TEMPLATE 2.25, 2.5, 2.75	
Slip (km)	Net Slip (km)	Time (Ma)	Velocity (mm/yr)	Time (Ma)	Velocity (mm/yr)	Time (Ma)	Velocity (mm/yr)
0.0	0.0	23.00	N/A	23.00	N/A	20.00	N/A
10.0	10.0	22.42	17.28	22.68	31.60	19.53	21.07
10.0	20.0	21.84	17.28	22.37	31.60	19.05	21.07
10.0	30.0	21.26	17.28	22.05	31.60	18.58	21.07
10.0	40.0	20.68	17.28	21.73	31.60	18.10	21.07
10.0	50.0	20.11	17.28	21.42	31.60	17.63	21.07
13.2	63.2	19.34	17.28	21.00	31.60	17.00	21.07
10.0	73.2	18.76	17.28	20.32	14.65	16.54	21.98
10.4	83.6	18.16	17.28	19.61	14.65	16.07	21.98
10.0	93.6	17.58	17.28	18.92	14.65	15.62	21.98
4.5	98.1	17.32	17.28	18.62	14.65	15.41	21.98
10.0	108.1	16.74	17.28	17.94	14.65	14.96	21.98
10.0	118.1	16.16	17.28	17.25	14.65	14.50	21.98
10.0	128.1	15.59	17.28	16.57	14.65	14.05	21.98
10.0	138.1	15.01	17.28	15.89	14.65	13.59	21.98
13.0	151.1	14.25	17.28	15.00	14.65	13.00	21.98
10.0	161.1	13.68	17.28	14.76	41.28	12.86	69.42
10.0	171.1	13.10	17.28	14.52	41.28	12.71	69.42
10.0	181.1	12.52	17.28	14.27	41.28	12.57	69.42
10.0	191.1	11.94	17.28	14.03	41.28	12.42	69.42
5.0	196.1	11.65	17.28	13.91	41.28	12.35	69.42
10.0	206.1	11.07	17.28	13.67	41.28	12.21	69.42
11.7	217.8	10.39	17.28	13.38	41.28	12.04	69.42
10.0	227.8	9.82	17.28	13.14	41.28	11.90	69.42
4.5	232.3	9.56	17.28	13.03	41.28	11.83	69.42
10.0	242.3	8.98	17.28	12.79	41.28	11.69	69.42
10.0	252.3	8.40	17.28	12.55	41.28	11.54	69.42
4.5	256.8	8.14	17.28	12.44	41.28	11.48	69.42
10.0	266.8	7.56	17.28	12.20	41.28	11.33	69.42
13.2	280.0	6.79	17.28	11.88	41.28	11.14	69.42
10.0	290.0	6.22	17.28	11.64	41.28	11.00	69.42
12.0	302.0	5.52	17.28	11.34	41.28	10.83	69.42
10.0	312.0	4.94	17.28	11.10	41.28	10.68	69.42
11.0	323.0	4.31	17.28	10.84	41.28	10.52	69.42
10.5	333.5	3.70	17.28	10.58	41.28	10.37	69.42
8.5	342.0	3.21	17.28	10.38	41.28	10.25	69.42
10.0	352.0	2.63	17.28	10.13	41.28	8.40	5.40
5.5	357.5	2.31	17.28	10.00	41.28	7.38	5.40
5.5	363.0	1.99	17.28	8.62	3.99	6.36	5.40
10.0	373.0	1.41	17.28	6.12	3.99	4.51	5.40
11.0	384.0	0.78	17.28	3.36	3.99	2.48	5.40
13.4	397.4	0.00	17.28	0.00	3.99	0.00	5.40

COLOR CODE

MAIN CENTRAL THRUST
SHUMAR THRUST
KAKHTANG THRUST
UPPER LH DUPLEX
MAIN BOUNDARY THRUST
MAIN FRONTAL THRUST

b) Split KT models

<b>VELOCITY: TOPOGRAPHY: Ao (<math>\mu\text{W}/\text{m}^3</math>):</b>		<i>CONSTANT</i> <i>PYTHON, TEMPLATE, NIL</i> 1.0, 2.0, 2.5, 3.0		<i>VELOCITY A</i> <i>PYTHON, TEMPLATE, NIL</i> 2.25, 2.5, 3.0		<i>VELOCITY B</i> <i>PYTHON, TEMPLATE, NIL</i> 2.25, 2.5, 3.0		<i>VELOCITY C</i> <i>PYTHON, TEMPLATE, NIL</i> 2.25, 2.5, 3.0	
Slip (km)	Net Slip (km)	Time (Ma)	Velocity (mm/yr)	Time (Ma)	Velocity (mm/yr)	Time (Ma)	Velocity (mm/yr)	Time (Ma)	Velocity (mm/yr)
0.0	0.0	23.00	N/A	23.00	N/A	20.00	N/A	20.00	N/A
10.0	10.0	22.42	17.28	22.68	31.60	19.53	21.07	19.53	21.07
10.0	20.0	21.84	17.28	22.37	31.60	19.05	21.07	19.05	21.07
10.0	30.0	21.26	17.28	22.05	31.60	18.58	21.07	18.58	21.07
10.0	40.0	20.68	17.28	21.73	31.60	18.10	21.07	18.10	21.07
10.0	50.0	20.11	17.28	21.42	31.60	17.63	21.07	17.63	21.07
13.2	63.2	19.34	17.28	21.00	31.60	17.00	21.07	17.00	21.07
10.0	73.2	18.76	17.28	20.32	14.65	16.60	25.11	16.60	25.11
10.4	83.6	18.16	17.28	19.61	14.65	16.19	25.11	16.19	25.11
10.0	93.6	17.58	17.28	18.92	14.65	15.79	25.11	15.79	25.11
4.5	98.1	17.32	17.28	18.62	14.65	15.61	25.11	15.61	25.11
10.0	108.1	16.74	17.28	17.94	14.65	15.21	25.11	15.21	25.11
10.0	118.1	16.16	17.28	17.25	14.65	14.81	25.11	14.81	25.11
10.0	128.1	15.59	17.28	16.57	14.65	14.42	25.11	14.42	25.11
10.0	138.1	15.01	17.28	15.89	14.65	14.02	25.11	14.02	25.11
13.0	151.1	14.25	17.28	15.00	14.65	13.50	25.11	13.50	25.11
10.0	161.1	13.68	17.28	14.73	37.28	13.37	74.56	12.90	16.67
10.0	171.1	13.10	17.28	14.46	37.28	13.23	74.56	12.30	16.67
5.0	176.1	12.81	17.28	14.33	37.28	13.16	74.56	12.00	16.67
10.0	186.1	12.23	17.28	14.06	37.28	13.03	74.56	11.85	64.56
11.7	197.8	11.55	17.28	13.75	37.28	12.87	74.56	11.66	64.56
10.0	207.8	10.97	17.28	13.48	37.28	12.74	74.56	11.51	64.56
4.5	212.3	10.71	17.28	13.36	37.28	12.68	74.56	11.44	64.56
10.0	222.3	10.13	17.28	13.09	37.28	12.55	74.56	11.28	64.56
10.0	232.3	9.56	17.28	12.82	37.28	12.41	74.56	11.13	64.56
4.5	236.8	9.29	17.28	12.70	37.28	12.35	74.56	11.06	64.56
10.0	246.8	8.72	17.28	12.43	37.28	12.22	74.56	10.90	64.56
13.2	260.0	7.95	17.28	12.08	37.28	12.04	74.56	10.70	64.56
10.0	270.0	7.37	17.28	11.81	37.28	11.91	74.56	10.55	64.56
12.0	282.0	6.68	17.28	11.49	37.28	11.74	74.56	10.36	64.56
10.0	292.0	6.10	17.28	11.22	37.28	11.61	74.56	10.20	64.56
11.0	303.0	5.46	17.28	10.93	37.28	11.46	74.56	10.03	64.56
10.5	313.5	4.86	17.28	10.64	37.28	11.32	74.56	9.87	64.56
8.5	322.0	4.36	17.28	10.42	37.28	11.21	74.56	9.74	64.56
10.0	332.0	3.79	17.28	10.15	37.28	11.07	74.56	9.59	64.56
5.5	337.5	3.47	17.28	10.00	37.28	11.00	74.56	9.50	64.56
10.0	347.5	2.89	17.28	8.33	5.99	9.16	5.45	8.42	9.22
10.0	357.5	2.31	17.28	6.66	5.99	7.33	5.45	7.33	9.22
5.5	363.0	1.99	17.28	5.74	5.99	6.32	5.45	6.32	5.44
10.0	373.0	1.41	17.28	4.07	5.99	4.48	5.45	4.48	5.44
11.0	384.0	0.78	17.28	2.24	5.99	2.46	5.45	2.46	5.44
13.4	397.4	0.00	17.28	0.00	5.99	0.00	5.45	0.00	5.44

COLOR CODE

MAIN CENTRAL THRUST
SHUMAR THRUST
KAKHTANG THRUST
UPPER LH DUPLEX
MAIN BOUNDARY THRUST
MAIN FRONTAL THRUST

c) Late KT models

<b>VELOCITY: TOPOGRAPHY: Ao (<math>\mu\text{W}/\text{m}^3</math>):</b>		<i>CONSTANT PYTHON, TEMPLATE 2.0, 2.5, 3.0, 3.5</i>		<i>VELOCITY A PYTHON, TEMPLATE 2.25, 2.5, 2.75, 3.0, 3.25, 3.5</i>		<i>VELOCITY B PYTHON, TEMPLATE 2.25, 2.5, 2.75, 3.0, 3.25, 3.5</i>	
Slip (km)	Net Slip (km)	Time (Ma)	Velocity (mm/yr)	Time (Ma)	Velocity (mm/yr)	Time (Ma)	Velocity (mm/yr)
0.0	0.0	23.00	N/A	23.00	N/A	20.00	N/A
10.0	10.0	22.42	17.28	22.68	31.60	19.53	21.07
10.0	20.0	21.84	17.28	22.37	31.60	19.05	21.07
10.0	30.0	21.26	17.28	22.05	31.60	18.58	21.07
10.0	40.0	20.68	17.28	21.73	31.60	18.10	21.07
10.0	50.0	20.11	17.28	21.42	31.60	17.63	21.07
13.2	63.2	19.34	17.28	21.00	31.60	17.00	21.07
10.0	73.2	18.76	17.28	20.32	14.65	16.54	21.98
10.4	83.6	18.16	17.28	19.61	14.65	16.07	21.98
10.0	93.6	17.58	17.28	18.92	14.65	15.62	21.98
4.5	98.1	17.32	17.28	18.62	14.65	15.41	21.98
10.0	108.1	16.74	17.28	17.94	14.65	14.96	21.98
10.0	118.1	16.16	17.28	17.25	14.65	14.50	21.98
10.0	128.1	15.59	17.28	16.57	14.65	14.05	21.98
10.0	138.1	15.01	17.28	15.89	14.65	13.59	21.98
13.0	151.1	14.25	17.28	15.00	14.65	13.00	21.98
10.0	161.1	13.68	17.28	14.76	41.28	12.86	72.95
11.7	172.8	13.00	17.28	14.47	41.28	12.70	72.95
10.0	182.8	12.42	17.28	14.23	41.28	12.57	72.95
4.5	187.3	12.16	17.28	14.12	41.28	12.50	72.95
10.0	197.3	11.58	17.28	13.88	41.28	12.37	72.95
10.0	207.3	11.00	17.28	13.64	41.28	12.23	72.95
4.5	211.8	10.74	17.28	13.53	41.28	12.17	72.95
10.0	221.8	10.16	17.28	13.29	41.28	12.03	72.95
13.2	235.0	9.40	17.28	12.97	41.28	11.85	72.95
10.0	245.0	8.82	17.28	12.73	41.28	11.71	72.95
12.0	257.0	8.13	17.28	12.43	41.28	11.55	72.95
10.0	267.0	7.55	17.28	12.19	41.28	11.41	72.95
11.0	278.0	6.91	17.28	11.93	41.28	11.26	72.95
10.5	288.5	6.30	17.28	11.67	41.28	11.12	72.95
8.5	297.0	5.81	17.28	11.47	41.28	11.00	72.95
10.0	307.0	5.23	17.28	11.22	41.28	10.78	45.00
10.0	317.0	4.65	17.28	10.98	41.28	10.56	45.00
10.0	327.0	4.07	17.28	10.74	41.28	10.33	45.00
10.0	337.0	3.50	17.28	10.50	41.28	10.11	45.00
5.0	342.0	3.21	17.28	10.38	41.28	10.00	45.00
10.0	352.0	2.63	17.28	10.13	41.28	8.19	5.54
5.5	357.5	2.31	17.28	10.00	41.28	7.20	5.54
5.5	363.0	1.99	17.28	8.62	3.99	6.21	5.54
10.0	373.0	1.41	17.28	6.12	3.99	4.40	5.54
11.0	384.0	0.78	17.28	3.36	3.99	2.42	5.54
13.4	397.4	0.00	17.28	0.00	3.99	0.00	5.54

COLOR CODE

MAIN CENTRAL THRUST
SHUMAR THRUST
KAKHTANG THRUST
UPPER LH DUPLEX
MAIN BOUNDARY THRUST
MAIN FRONTAL THRUST

## BIBLIOGRAPHY

- Adlakha, V.A., K.A. Lang, R.C. Patel, N. Lal, K.W. Huntington, 2013. Rapid long-term erosion in the rain shadow of the Shillong Plateau, Eastern Himalaya, *Tectonophysics*. 582, 76–83.
- Banerjee, P., and R. Burgmann, 2002. Convergence across the northwest Himalaya from GPS measurement, *Geophys. Res. Lett.*, 29(13), 1652.
- Banerjee, P., R. Burgmann, B. Nagarajan, and E. Apel, 2008. Intraplate deformation of the Indian subcontinent, *Geophys. Res. Lett.*, 35, L18301.
- Batt, G. E., and M. T. Brandon, 2002. Lateral thinking: 2-D interpretation of thermochronology in convergent orogenic settings, *Tectonophysics*, 349, 185 – 201.
- Berthet, T., G. Hetényi, R. Cattin, S.N. Sapkota, C. Champollion, T. Kandel, E. Doerflinger, D. Drukpa, S. Lechmann, and M. Bonnin, 2013. Lateral uniformity of India Plate strength over central and eastern Nepal, *Geophys J. Int*, 195(3), 1481-1493.
- Bettinelli, P., J. P. Avouac, M. Flouzat, F. Jouanne, L. Bollinger, P. Willis, and G. R. Chitrakar, 2006. Plate motion of India and interseismic strain in the Nepal Himalaya from GPS and DORIS measurements, *J. Geod.*, 80, 567–589.
- Bhargava, O. N., 1995. The Bhutan Himalaya: A Geological Account, *Spec. Publ. Ser. Geol. Surv. India*, 39, 245 pp.
- Bilham, R., K. Larson, J. Freymueller, and Project Idylhim Members, 1997. GPS measurements of present-day convergence across the Nepal Himalaya, *Nature*, 386, 61–64.
- Braun, J., 2003. Pecube: a new finite-element code to solve the 3D heat transport equation including the effects of a time-varying, finite amplitude surface topography, *Computers & Geosciences*, 29, 787-794.
- Burbank, D.W., 2005. Cracking the Himalaya. *Nature*, 434, 963-964.
- Célérier, J., T.M. Harrison, O. Beyssac, F. Herman, W.J. Dunlap, and A.G. Webb, 2009. The Kumaun and Garwhal Lesser Himalaya, India. Part 2: Thermal and deformation histories, *Geol Soc. Am. Bull.*, 121, 1281-1297.

- Coutand, I., D.M. Whipp Jr., D. Grujic, M. Bernet, M.G. Fellin, B. Bookhagen, K.R. Landry, S.K. Ghalley, C. Duncan, 2014. Geometry and kinematics of the Main Himalayan Thrust and Neogene crustal exhumation in the Bhutanese Himalaya derived from inversion of multithermochronologic data, *J. Geophys. Res., Solid Earth*, 119.
- Davidson, C., D. E. Grujic, L. S. Hollister, and S. M. Schmid, 1997. Metamorphic reactions related to decompression and synkinematic intrusion of leucogranite, High Himalayan crystallines, Bhutan, *J. Metamorph. Geol.*, 15, 593–612.
- DeCelles, P.G., D.M. Robinson, J. Quade, T.P. Ojha, C.N. Garzione, P. Copeland, B.N. Upreti, 2001. Stratigraphy, structure, and tectonic evolution of the Himalayan fold–thrust belt in western Nepal, *Tectonics*, 20, 487–509.
- DeCelles, P. G., D. M. Robinson, and G. Zandt, 2002. Implications of shortening in the Himalayan fold-thrust belt for uplift of the Tibetan Plateau, *Tectonics*, 21(6), 1062.
- Duncan, C., J. Masket, and E. Fielding, 2003. How steep are the Himalaya? Characteristics and implications along-strike topographic variations, *Geology*, 31, 75–78.
- Ehlers, T.A., and K.A. Farley, 2003. Apatite (U–Th)/He thermochronometry; methods and applications to problems in tectonic and surface processes, *Earth Planet. Sci. Lett.*, 206, 1–14.
- England, P., P. Le Fort, P. Molnar, and A. Pêcher, 1992. Heat sources for Tertiary metamorphism and anatexis in the Annapurna–Manaslu region (central Nepal), *J. Geophys. Res.*, 97, 2107–2128.
- Gansser, A., 1964. *Geology of the Himalayas*, 289 pp., Wiley-Interscience, New York.
- Gansser, A., 1983. *Geology of the Bhutan Himalaya*, 181 pp., Birkäuser, Basel.
- Grujic, D., L. S. Hollister, and R. R. Parrish, 2002. Himalayan metamorphic sequence as an orogenic channel: Insight from Bhutan, *Earth Planet. Sci. Lett.*, 198, 177–191.
- Grujic, D., I. Coutand, B. Bookhagen, S. Bonnet, A. Blythe, and C. Duncan, 2006. Climatic forcing of erosion, landscape, and tectonics in the Bhutan Himalayas, *Geology*, 34, 801–804.
- Hammer, P., T. Berthet, G. Hetényi, R. Cattin, D. DRupka, J. Chophel, S. Lechmann, N. Le Moigne, C. Champollion, and E. Doerflinger, 2013. Flexure of the India plate underneath the Bhutan Himalaya, *Geophys. Res. Lett.*, 40(16), 4225–4230.
- Heim, A., and A. Gansser, 1939, Central Himalayas—Geological observations of Swiss expedition, 1936, *Mem. Soc. Helv. Sci. Nat.*, 73, 1–245.
- Herman, F., P. Copeland, J.P. Avouac, L. Bollinger, G. Mahéo, P. Le Fort, S. Rai, D. Foster, A. Pêcher, K. Stüwe, and P. Henry, 2010. Exhumation, crustal deformation, and thermal

- structure of the Nepal Himalaya derived from the inversion of thermo-chronological and thermobarometric data and modeling of the topography, *J. Geophys. Res.*, 115, B06407.
- Hodges, K.V., R.R. Parrish, R.R., and M.P. Searle, 1996. Tectonic evolution of the central Annapurna Range, Nepalese Himalayas: *Tectonics*, v. 15, p. 1264–1291.
- Hodges, K. V., 2000. Tectonics of the Himalaya and southern Tibet from two perspectives, *Geol. Soc. Am. Bull.*, 112, 324–350.
- Hollister, L. S., and D. Grujic, 2006. Pulsed channel flow in Bhutan, *Geol. Soc. Spec. Publ.*, 268, 415–423.
- Huntington, K.W., T.A. Ehlers, K.V. Hodges, and D.M. Whipp Jr., 2007. Topography, exhumation pathway, age uncertainties, and the interpretation of thermochronometer ages, *Tectonics*, 26, TC4012.
- Jain, A.K., D. Kumar, S. Singh, A. Kumar, and N. Lal, 2000. Timing, quantification and tectonic modelling of Pliocene–Quaternary movements in the NW Himalaya: Evidence from fission track dating. *Earth Planet. Sci. Lett.*, 179, 437–451.
- Larson, K. M., R. Burgmann, R. Bilham, and J. Freymueller, 1999. Kinematics of the India-Eurasia collision zone from GPS measurements, *J. Geophys. Res.*, 104, 1077–1093.
- Lavé, J., and J. P. Avouac, 2000. Active folding of fluvial terraces across the Siwaliks Hills, Himalayas of central Nepal, *J. Geophys. Res.*, 105, 5735–5770.
- LeFort, P., 1975. Himalayas: The collided range, present knowledge of the continental arc, *American Journal of Science*, 275-A, 1–44.
- Long, S., and N. McQuarrie, 2010. Placing limits on channel flow: Insights from the Bhutan Himalaya, *Earth Planet. Sci. Lett.*, 290, 375–390.
- Long, S., N. McQuarrie, T. Tobgay, and D. Grujic, 2011a. Geometry and crustal shortening of the Himalayan fold-thrust belt, eastern and central Bhutan, *Geol. Soc. Am. Bull.*, 123, 1427–1447.
- Long, S., N. McQuarrie, T. Tobgay, C. Rose, G. Gehrels, and D. Grujic, 2011b, Tectonostratigraphy of the Lesser Himalaya of Bhutan: Implications for the along-strike stratigraphic continuity of the northern Indian margin, *Geol. Soc. Am. Bull.*, 123, 1406–1426.
- Long, S.P., N. McQuarrie, T. Tobgay, I. Coutand, F. Cooper, P. Reiners, J. Wartho, and K.V. Hodges, 2012. Variable shortening rates in the eastern Himalayan thrust belt, Bhutan: insights from multiple thermochronologic and geochronologic datasets tied to kinematic reconstructions, *Tectonics*, 31, TC5004.

- Mattauer, M., 1986. Intracontinental subduction, crust-mantle décollement and crustal-stacking wedge in the Himalayas and other collision belts, in *Collision Tectonics*, edited by M. P. Coward and A. C. Ries, *Geol. Soc. Spec. Publ.*, 19, 37–50.
- McQuarrie, N., D. Robinson, S. Long, T. Tobgay, D. Grujic, G. Gehrels, and M. Ducea, 2008. Preliminary stratigraphic and structural architecture of Bhutan: Implications for the along-strike architecture of the Himalayan system, *Earth Planet. Sci. Lett.*, 272, 105–117.
- McQuarrie, N., and T. Ehlers, 2013. Integrating kinematic and thermal models to quantify magnitude and variability in rates of faulting through the eastern Himalaya: Abstract T34B-05, presented at 2013 Fall Meeting, AGU, San Francisco, Calif., 9-13 Dec.
- McQuarrie, N., T. Tobgay, S.P. Long, P.W. Reiners, and M.A. Cosca, 2014. Variable exhumation rates and variable displacement rates: documenting a recent slowing of Himalayan shortening in western Bhutan, *Earth Planet. Sci. Lett.*, 386, 161-174.
- McQuarrie, N. and T. Ehlers, 2014. The Influence of Geometry and Rates of Thrusting on Thermochronometer Cooling Ages: Insights from the Bhutan Himalaya. Manuscript in preparation.
- Menon, R., P. Kumar, G. Reddy, and R. Srinivasan, 2003, Radiogenic heat production of late Archaean Bundelkhand granite and some Protero- zic gneisses and granitoids of central India, *Curr. Sci.*, 85, 634–638.
- Mitra, S., K. Priestley, A. Bhattacharyya, and V.K. Gaur, 2005. Crustal structure and earthquake focal depths beneath northeastern India and southern Tibet, *Geophys. J. Int.*, 160, 227–248.
- Patriat, P., and J. Achache, 1984. Indian-Eurasian collision chronology has implications for crustal shortening and driving mechanisms of plates, *Nature*, 311, 615– 621.
- Powell, C.M., and Conaghan, P.J., 1973. Plate tectonics and the Himalayas, *Earth Planet. Sci. Lett.* 20, 1–12.
- Ray, L., Bhattacharya, A., and Roy, S., 2007. Thermal conductivity of Higher Himalayan Crystallines from Garhwal Himalaya, India. *Tectonophysics* 434, 71–79.
- Robert, X., P. van der Beek, J. Braun, C. Perry, M. Dubille, and J.-L. Mugnier, 2009. Assessing Quaternary reactivation of the Main Central Thrust zone (central Nepal Himalaya): New thermochronologic data and numerical modeling, *Geology*, 37(8), 731–734.
- Robinson, D.M., and N. McQuarrie, 2012. Pulsed deformation and variable slip rates in the Central Himalayan Thrust Belt, *Lithosphere* 4, 449–464.
- Stüwe, K., and D. Foster, 2001.  $^{40}\text{Ar}/^{39}\text{Ar}$ , pressure, temperature and fission track constraints on the age and nature of metamorphism around the Main Central Thrust in the eastern Bhutan Himalaya, *J. Asian Earth Sci.*, 19(1–2), 85–95.

- Thiede, R., T.A. Ehlers, B. Bookhagen, M.R. Strecker, 2009. Erosional variability along the northwest Himalayan Front, *J. Geophys. Res., Earth Surface*, 114, F01015.
- Thiede, R. C., and T. A. Ehlers, 2013, Large spatial and temporal variations in Himalayan denudation, *Earth Planet. Sci. Lett.*, 371, 278-293.
- Whipp, D.M. Jr., T.A. Ehlers, A.E. Blythe, K.W. Huntington, K.V. Hodges, and D.W. Burbank, 2007. Plio-quaternary exhumation history of the central Nepalese Himalaya: 2. Thermokinematic and thermochronometer age prediction model, *Tectonics*, 26, TC3003.
- Whipp, D., T. Ehlers, J. Braun, and C. Spath, 2009. Effects of exhumation kinematics and topographic evolution on detrital thermochronometer data, *Journal of Geophysical Research* 114, F04021.
- Wobus, C.W., K.V. Hodges, and K.X. Whipple, 2003. Has focused denudation sustained active thrusting at the Himalayan topographic front?, *Geology*, 31(10), 861-864.
- Yin, A., 2006. Cenozoic tectonic evolution of the Himalayan orogen as constrained by along-strike variation of structural geometry, exhumation history, and foreland sedimentation, *Earth Sci. Rev.*, 76, 1–131.
- Yin, A., and T.M. Harrison, 2000. Geologic evolution of the Himalayan-Tibetan orogeny, *Annual Review of Earth and Planetary Sciences*, 28, 211–280.
- Zhang, P. Z., et al., 2004. Continuous deformation of the Tibetan Plateau from global positioning system data, *Geology*, 32, 809–812.